FREQUENCY DOMAIN COMPUTATION OF TURBOFAN EXHAUST NOISE RADIATION

A THESIS SUBMITTED TO
THE GRADUATE SCHOOL OF NATURAL AND APPLIED SCIENCES
OF
MIDDLE EAST TECHNICAL UNIVERSITY

BY

YAVUZ BARBAROS ULUSOY

IN PARTIAL FULFILLMENT OF THE REQUIREMENTS

FOR

THE DEGREE OF MASTER OF SCIENCE

IN

AEROSPACE ENGINEERING

APRIL 2006

Approval of the Graduate School of Natural and Applied Sciences.

Prof. Dr. Canan Özgen
Director

I certify that this thesis satisfies all the requirements as a thesis for the degree of Master of Science.

Prof. Dr. Nafiz Alemdaroğlu
Head of Department

This is to certify that we have read this thesis and that in our opinion it is fully adequate, in scope and quality, as a thesis for the degree of Master of Science.

Prof. Dr. Yusuf Özyörük
Supervisor

Examining Committee Members

Prof. Dr. İ. Sinan Akmandor (METU, AEE)

Prof. Dr. Yusuf Özyörük (METU, AEE)

Prof. Dr. İsmail H. Tuncer (METU, AEE)

Prof. Dr. Haluk Aksel (METU, ME)

Assoc. Prof. Sinan Eyi (METU, AEE)

I hereby declare that all information in this document has been obtained and presented in accordance with academic rules and ethical conduct. I also declare that, as required by these rules and conduct, I have fully cited and referenced all material and results that are not original to this work.

Name, Last Name:

Signature:

ABSTRACT

FREQUENCY DOMAIN COMPUTATION OF TURBOFAN EXHAUST NOISE RADIATION

Ulusoy, Yavuz Barbaros

M.S., Department of Aerospace Engineering

Supervisor: Prof. Dr. Yusuf Özyörük

April 2006, 71 pages

In this study, acoustic noise radiation through a duct in frequency domain is analyzed. Frequency domain linearized Euler equations are solved for turbofan exhaust noise propagation and radiation. The geometry in studied cases is assumed as axisymmetric. The acoustic waves are decomposed into periodic azimuthal modes. Characteristic boundary conditions, and buffer zone boundary conditions are employed. Iterative type pseudo time integration is employed. Nonuniform background flow effect on the radiation pattern is experienced. All computations are performed in parallel using MPI library routines in computer cluster. Results proved that the one with the buffer zone has a better radiation characteristic than the characteristic one because of absorbtion of spurious waves. It is seen that the efficiency of the buffer zone is frequency dependent.

Keywords: Aerodynamic Noise, Turbofan Noise Radiation, Parallel Processing, Frequency Domain, Linearized Euler Equation, Buffer Zone, Non-reflecting Boundary Conditions

ÖZ

TURBOFAN MOTORLARIN ARKA KISMINDAN YAYILAN SESİN FREKANS ALANINDA SİMULASYONU

Ulusoy, Yavuz Barbaros
Yüksek Lisans, Havacılık ve Uzay Mühendisliği Bölümü
Tez Yöneticisi: Prof. Dr. Yusuf Özyörük

Nisan 2006, 71 sayfa

Bu çalışmada, bir borudan yayılan akustik ses frekans kümesinde incelendi. Frekans kümesindeki doğrusallaştrılmış Euler denklemleri turbofan egzoz ses dağılımı ve yayılımı için çözüldü. Sayısal uygulamalarda çalışılan geometri eksenel simetrik olarak alındı. Akustik dalgalar periyodik ufki modlara ayrıştırıldı. Karakteristik ve tampon sınır şartları uygulandı. Tekrarlayıcı tipinde takma zaman integrali kullanıldı. Düzensiz arka plan akışın yayılım paternine etkisi gözlemlendi. Tüm hesaplamalar paralel MPI kütüphanesi kullanılarak bilgisayar kümesinde yapıldı. Sonuçlar şunu gösterdi ki ; tampon bölge şartları uygulanarak yapılan çalışmalardaki yayılma paterni karakteristik şartlarla elde edilenlerden daha iyi. Tampon bölgenin veriminin cut-off oranına bağlı olduğu görüldü.

Anahtar Kelimeler: Ayrodinamik Ses, Turbofan Ses Yayılımı , frekans alanı, Paralel İşlemler, Doğrusallaştırılmış Euler Denklemleri, Tampon Bölge, Yansıtıcı olmayan Sınır Şartları

to my family...

ACKNOWLEDGMENTS

I want to state my thanks to

My thesis supervisor *Assoc. Prof. Dr. Yusuf Özyörük* for his guidance and valuable sharing in our study of CFD with me through this study with patience. Although we faced with difficulties in this study, we get rid of them with a big success.

My parents for their advice and supports in my life, being with me anytime and anywhere that I need help, sharing the light we consider to reach all the time. My father , my mother, my sister, my uncle, my aunts, my cousins for their love, smile.My grandmother, glancing at me from the stars, this is the success of me and you, including the ten years tiring and wonderful time with you.

My assistant friends I am still with you if you need help in exams. Mustafa Kaya, for his helps and jokes making me sick, sharing the knowledge in every area. Özgür Demir, Vahit wishing you not to have runlar yalan oldu period.

My instructors in the department for their answers to my questions and solutions to my problems, regardless of how silly and annoying they are.

My department for giving me a chance to be a graduate assistantship, which played a very important role during my studies.

My all friends you shouldn't misunderstand me that you are at the end of the page, this will never end. This undergraduate and graduate period of my life with you is the most valuable gift given to me in my life, reflecting sharing, wishing,warm heart and mind. We shared more time than we lived together. Ayhan, Ender, Evren, Fuat, Gencer, Mehmet, Serkan, Sertan, Tuğrul, Volkan, like a squad; here a time travel: Food Engineering basement reinforcement, the first use of roman candle in METU, Squash Tournaments, Henpecked positions, Football matches, Pink Letters, Facing the firsts in our life with you, METU festivals, confusions, last minute loading and unloading, refuelling, horse hippodrome, ice skiing, bir açık bir kapalı and plakadanmısınız in Mersin, tennis courts construction, the right hand side of our canteen. Also Eray, Koray Daye, Sertaç, Serkan Deveci, Emre Yüksel, Mert Bayat we will never forget us Barış Vural, during this little period, giving his everything to me other than sharing the same room in Etimesgut, fighting together to the silly restrictions, we may reach our dream to be a agricultural fire pilot (zuzu). And, Utku teaching me dance of knights.

PREFACE

The sound radiation became a vulnerable problem with developing industry. Researches on this area cleared some aspects of radiation problem. Today, although the developed methods are qualified the noise restrictions around some airports force researches to make more quiet models. Frequency domain proved its ability on impedance boundaries. Buffer zone applied in this study also help the method to make simulation more correctly.

I think the method applied will courage CFD heros to make more modern and up-to-date approaches to turbofan noise radiation simulation and suppression.

You can report all comments to the following e-mail address:

Yavuz Barbaros Ulusoy
ybu@ae.metu.edu.tr

All comments are welcome.

Y.B.U.

METU, Ankara

May 2006

TABLE OF CONTENTS

PLAGIARISM iii

ABSTRACT iv

ÖZ v

DEDICATON vi

ACKNOWLEDGMENTS vii

PREFACE viii

TABLE OF CONTENTS ix

LIST OF TABLES xi

LIST OF FIGURES xii

LIST OF SYMBOLS xiv

CHAPTER

- 1 INTRODUCTION 1
  - 1.1 Introduction 1
  - 1.2 Aeroacoustics 9
  - 1.3 Numerical Studies on Fan Noise 12
  - 1.4 Thesis Scope and Outline 19
- 2 NUMERICAL METHOD 21
  - 2.1 Introduction 21
  - 2.2 Governing Equations 21
    - 2.2.1 Linearized Euler Equation 21
  - 2.3 Boundary Conditions 23
    - 2.3.1 Fan-Face condition 23
      - 2.3.1.1 Acoustic source conditions 23
    - 2.3.2 Buffer Zone Approach 26
    - 2.3.3 Hard Wall Conditions 28
    - 2.3.4 Impedance Conditions 29
    - 2.3.5 Far-Field Conditions 30
    - 2.3.6 Discretization 31

- 2.3.7 Farfield Predictions . . . 32
- 2.3.8 Parallel Processing . . . 33

3 RESULTS AND DISCUSSION . . . 36
- 3.1 Introduction . . . 36
- 3.2 Mean Flow Calculations . . . 37
- 3.3 Acoustic field . . . 38
  - 3.3.1 Test of Duct Inlet Conditions . . . 38
  - 3.3.2 Acoustic Field with no Background Flow . . . 44
  - 3.3.3 Acoustic Field with Background Flow . . . 49
  - 3.3.4 Buffer Zone and Characteristic Based Boundary Conditions Application . . . 50
  - 3.3.5 Acoustic Field for a Mode of lower Cut-Off . . . 52
  - 3.3.6 Effect of Buffer Zone Length on Acoustic Field . . . 58
  - 3.3.7 Farfield Calculation for different Kirchhoff Surfaces . . . 60
  - 3.3.8 Effect of Background Flow on Acoustic Radiation . . . 62

4 CONCLUDING REMARKS . . . 65

REFERENCES . . . 68

LIST OF TABLES

TABLE

2.1 Parallel Computers used for the Project 34

LIST OF FIGURES

FIGURES

1.1 Jet Noise Schematic [54]. 2
1.2 Corrugated nozzle For Jet Noise Suppression [54]. 2
1.3 TF39 Turbofan Engine (Rolls-Royce Conway, Pratt Whitney JT3-D)[57]. 3
1.4 Departure and Arrival Noise Level Comparison [4]. 3
1.5 Turbojet / Turbofan Engine Component Noise Propagation Characteristic [4]. . 5
1.6 ICAO Annex 16 Certification, take-off and landing profile [55]. 5
1.7 The overall noise level decrement over the years [6]. 7
1.8 Attenuation with liners [56]. 7

2.1 Circular and Annular Duct Mode pattern for $m = 6$. 25
2.2 Annular Duct Mode pattern for $m = 13$. 25
2.3 Buffer zone in circular duct. 27
2.4 Kirchhoff Method 33
2.5 Parallel Computation. 33
2.6 Flow Chart for the parallel computation. 34

3.1 Computational Domain 37
3.2 Annular Duct Geometry 38
3.3 Constant cross section, thin walled annular duct. Upper half : long duct , lower half : short duct 39
3.4 Mean Flow Mach Number for annular duct 40
3.5 Normalized acoustic source profiles 40
3.6 Normalized acoustic source profiles 41
3.7 Acoustic fields of spinning mode $(6, 0)$ using long duct with buffer zone and short duct with characteristics based boundary conditions at 3120 Hz 42
3.8 Wave admission buffer zone in the duct 43
3.9 Acoustic fields of spinning mode $(13, 0)$ using long duct with buffer zone and short duct with characteristics based boundary conditions at 4320 Hz 43
3.10 Subdomains for Solution Domain 44
3.11 Acoustic field of mode $(10, 0)$, f=960 Hz, cut-off=1.82 45
3.12 Normalized acoustic source profile for $(10, 0)$ mode. 46
3.13 Kirchhoff Surface for mode $(10, 0)$ 46
3.14 Farfield Sound Pressure Levels for direct and frequency domain approaches for $(10, 0)$ mode, f=960 Hz 47
3.15 Kirchhoff Surface on Solution Mesh 48
3.16 Time Harmonic Propagation for mode $(10, 0)$, f=960 Hz (T= period of the wave) 48
3.17 Farfield directivity for mode $(10, 0)$, f=860 Hz, $R = 50$ m 49
3.18 Pressure for $(10, 0)$ mode, $f = 860$ Hz 50
3.19 Solution Domain 50
3.20 Normalized acoustic source profile for $(13, 0)$ mode 51
3.21 SPL for $(13, 0)$ mode, $f = 1250$ Hz, dashed line = buffer zone BCs, line= characteristic BCs 51
3.22 Radiation directivity for $(13, 0)$ mode, $f = 1250$ Hz, $R = 100$ m 52

3.23 Radiation directivity for $(13, 0)$ mode, $f = 1250$ Hz 52
3.24 Mesh for $(17, 0)$ mode. 53
3.25 Acoustic field of mode $(17, 0)$ at 870 Hz 54
3.26 Kirchhoff surface on the mesh for mode $(17, 0)$ 54
3.28 Kirchhoff surface pressure field for mode $(17, 0)$ 55
3.29 Farfield directivity of buffer zone and characteristic boundary conditions for $(17, 0)$ mode 55
3.27 Kirchhoff surface mesh for mode $(17, 0)$ 55
3.30 Instantaneous pressure field for mode $(17, 0)$ 56
3.31 Acoustic field of mode $(17, 0)$ at 870 Hz 57
3.32 Farfield directivity for $(17, 0)$mode, with buffer zone and characteristic boundary conditions 58
3.33 Mesh for $(17, 0)$ mode 59
3.34 Farfield Radiation for 3 selected buffer length 59
3.35 Farfield Radiation for 3 selected buffer length, zoomed at maximum amplitude . 60
3.36 3 Kirchhoff Surfaces,for $(10, 0)$ mode 60
3.37 Farfield directivity of 3 Kirchhoff Surfaces,for $(10, 0)$ mode, $R = 50$ m 61
3.38 Kirchhoff surface 1 pressure distribution,for $(10, 0)$ mode 61
3.39 Kirchhoff surface 2 pressure distribution,for $(10, 0)$ mode 61
3.40 Kirchhoff surface 3 pressure distribution,for $(10, 0)$ mode 62
3.41 Normalized acoustic source profile for $(9, 0)$ mode 63
3.42 Mean flow Mach number distribution 63
3.43 Farfield directivity of mode $(9, 0)$ with diffused shear layer, R=50m 64
3.44 Farfield directivity of diffused and infinitely long shear layer with buffer zone, R=50m 64

LIST OF SYMBOLS

ROMAN SYMBOLS

B	Number of rotor blades
c	Speed of sound
D	Artificial dissipation
f	Frequency in Hertz
i	Complex number, $\sqrt{-1}$
J_m	m^{th} order Bessel Function of first kind
J'_m, Y'_m	derivatives of Bessel Functions with respect to r
k	Wave number
L_{ref}	Length of Buffer zone
m	Azimuthal mode
M	Mach Number
n	Time harmonic index
r	Radial distance in Cylindrical system
R	Residual matrix, Radius of wall curvature
S	Kirchhoff surface
Q	Solution matrix
t	Time
u	Velocity component in x-direction
Y_m	m^{th} Bessel Function of second kind
v	Velocity component in y-direction
V	Number of stator vanes
w	Velocity component in z-direction
x, y, z	Spatial coordinates in Cartesian system

GREEK SYMBOLS

$\Re$	Real part of the variable
γ	Specific heat ratio
θ	Angular coordinate in Cylindrical system
ω	Circular frequency
ρ	Density
μ	Radial mode
σ	Hub to tip ratio
$\sigma(x)$	Transition coefficient
ξ	Cut-off ratio
τ	Pseudo term; source emission time
ξ, η	Spatial coordinates in computational domain
$\xi_x, \xi_z, \eta_x, \eta_z$	Metrics of transformation

SUBSCRIPTS

∞	Freestream value
0	Mean flow quantitiy
inc	Incident field
n	Normal component of velocity
t	Tangential component of velocity

SUPERSCRIPTS

$'$	Perturbation
$\widehat{\ }$	Complex quantity, Incident field variables
$+$	Acoustic Wave going in downstream direction

CHAPTER 1

INTRODUCTION

1.1 Introduction

Until World War II, propellers constituted the only means of propulsion in aviation. Effective roles of aircrafts in war have changed its shape to humanity. After the war, the world goes into an industrial evolution. Over 5 years, aircraft industry shows a magnificent change. Experience gained during the war helped researchers to improve. They tried to have high performance aircraft with the invention of turbojet engine. Meanwhile, it became clear that the recently developed jet propulsion technology offered numerous advantages over propellers. For various reasons, the conventional propellers never disappeared altogether. For general aviation and commuter aircraft, propellers are still widely used. Besides, it seems like to not to disappear from the aviation [1].

The performance criteria of this era were aerodynamic and propulsive. Enhancements in the aviation technology also exposed some problems to humanity. These aircrafts, in the late 1950s, were powered mainly by military aircraft propulsion units,turbojets. Turbojet working principle can be summarized briefly as breathing in air with inlet duct, compressing it with compressor, mixing fuel with the compressed air and igniting the mixture with combustion chambers, after extracting energy to drive the compressor through a set of turbine blades releasing the gas into the atmosphere through a nozzle as a hot jet with a high velocity. At the exhaust region, both

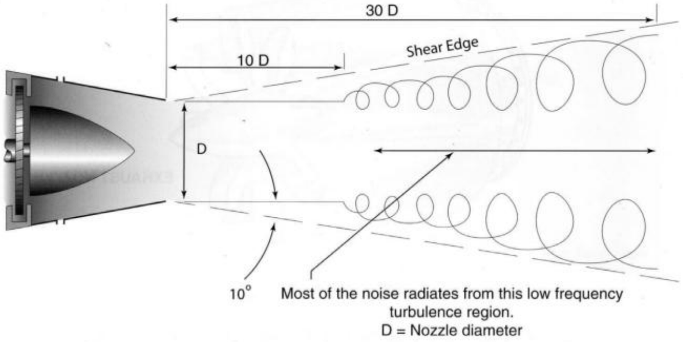

Figure 1.1: Jet Noise Schematic [54].

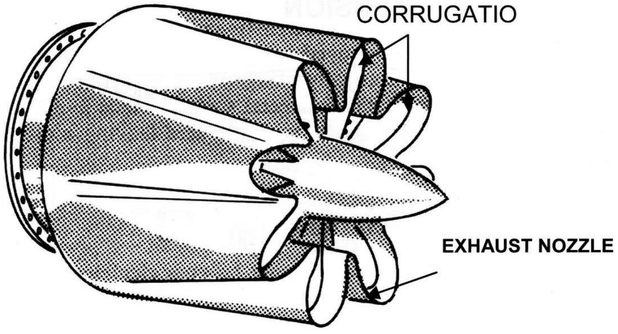

Figure 1.2: Corrugated nozzle For Jet Noise Suppression [54].

momentum and pressure are the products. But, the main product, a high jet exhaust velocity, causes a high level of what is termed "jet mixing noise" due to the mixing of the exhaust gas with the surrounding air. This is mainly due to turbulence, as in Figure 1.1. It was realized at the time that the noise levels produced by aircraft would be unacceptable to the persons living under the takeoff/landing pattern of major airports.

Takeoff noise restrictions were imposed by some airport managements and nearly all first-generation turbojet powered transports were equipped with jet noise suppressors, like corrugated nozzle in Figure 1.2. New generation Airbus aircrafts have this type of exhaust. But, this technique turned to operator at a significant cost in weight, thrust and fuel consumption. These lead the researchers to enhance in material and turbine cooling technology, allowing engine designers to move larger masses of air at lower exhaust velocities using bypass engines. The developing technology ended with the birth of first high-bypass turbofan engine shown in Figure 1.3, TF39. Opposite to turbojet engines, the airflow into the engine is divided into

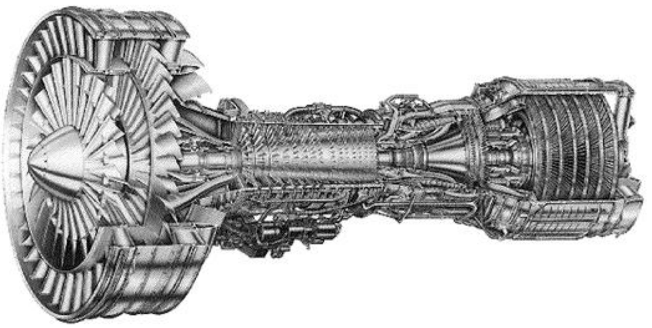

Figure 1.3: TF39 Turbofan Engine (Rolls-Royce Conway, Pratt Whitney JT3-D)[57].

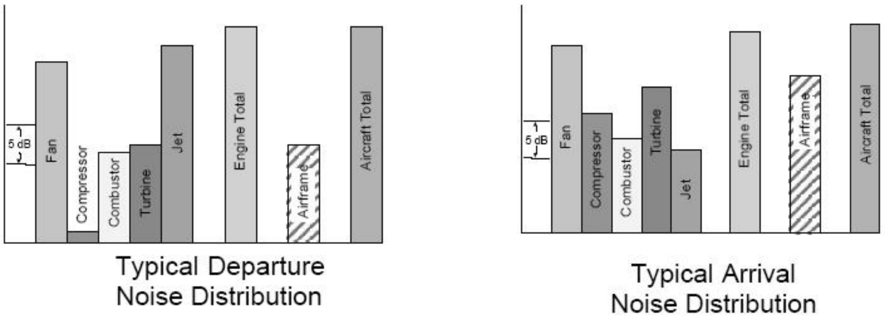

Figure 1.4: Departure and Arrival Noise Level Comparison [4].

two streams in turbofan engines; one of which bypasses the combustion process and exhaust into the atmosphere at a lower velocity and temperature than the free stream through the core of the engine. However, at high bypass ratios the energy extracted from the core stream can reduce that velocity to lower than the bypass stream velocity at some power condition. The introduction of the turbofan engine with its low jet velocity temporarily alleviated the jet noise but increased the high frequency turbomachinery noise, which became a severe problem on landing approach as well as takeoff [1], in Figure 1.4. This figure clarifies also turbulence effects in clean and landing configurations. Researchers are focused on two basic ideas; lowering the noise by source attenuation or by using acoustic treatments in engine duct. The former is reduced by understanding of the noise mechanism; numbers of stator and rotor blades, unsteady aerodynamic flow, inlet geometry shape, exhaust geometry shape, combustion instabilities. The latter are used in turbofan engine nacelles for the purpose of suppression of engine noise, liners. For a given turbofan engine there are different optimum impedance conditions corresponding to different operation conditions; take-off, cut-back, and approach flight. This can restrict the aircraft pilot with the flight regime conditions according to airdrome's restrictions. These necessitate active liners. They are located at the engine duct inside surface and provide an impedance boundary condition for the acoustic modes propagating within the duct. But as expected, this absorbing material can not reduce the level totally. Existing active liner technology offers adjustable liner impedance, but expected drawbacks in terms of cost, power consumption, wiring, weight are non-trivial [8].

For someone who is getting closer to a noise generating mechanism, the noise can be overcome by a simple earplug. However, this is not appropriate for people living near an airport. Annoyance, sleep disruption, hearing damage, speech interference, and decrease in productivity are all the effect of noise on human in impacted areas [49]. The more applicable and appropriate methods to reduce the generated noise are required. It should be noted that, while reducing the noise, some specified performance characteristics must still be satisfied. Most of the researches are currently focused on turbofan engine. Jet noise is significantly decreased with the turbofan engines. However, another source of noise is introduced due to fan. This fan noise generated has the most contribution to the overall noise. Past two decades, researchers mainly studied on this mechanism.

In addition to airframe noise, the main sources of noise from gas turbine engines can be listed as below. They are

- Jet noise
- Fan and compressor noise
- Core noise including combustion noise
- Turbine noise

Typical radiation pattern of noise from gas turbine engine from its components is shown in Figure 1.5. Their frequency spectrum differs in some respect.

Researchers working on the advance unducted aerodynamic researches showed that these advanced propellers have efficient aerodynamic characteristics, such as lower section Mach number, lower tip vortex strength, lower drag. Although their effectiveness enhance noise suppression

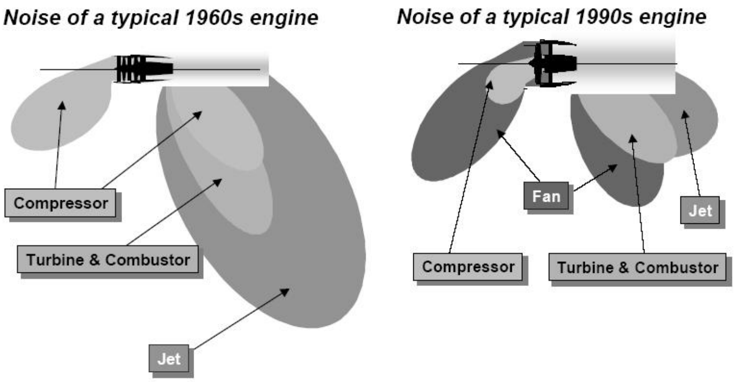

Figure 1.5: Turbojet / Turbofan Engine Component Noise Propagation Characteristic [4].

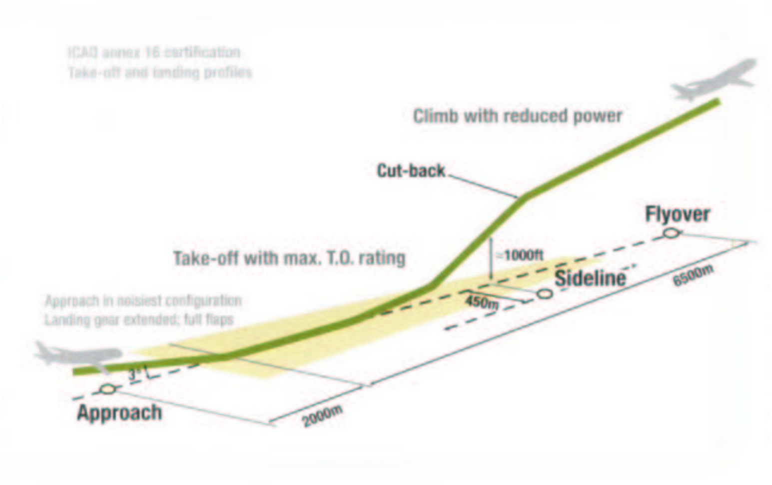

Figure 1.6: ICAO Annex 16 Certification, take-off and landing profile [55].

this is not enough to reduce the caused noise in the cabin. So ducted fan showed its inevitable advantage widely used despite these [19]. Acoustic radiation characteristic is also effected by the shape of the geometry covering the noise source. This is as important as ground clearance and producibility [20].

Public reaction to aircraft jet noise started especially during years 1960-1965. The first meeting constructing noise certification's future was in Montreal, on December 1969. First application of noise restrictions on new subsonic aeroplanes with a Maximum Take of Weight ,MTOW , greater than $34,000$ kg is applied on 1st December 1969. Application to all aeroplanes was on 31st December 1974 [5]. The time limitations and overcontinent trade in human life increased volume of air traffic resulted in unacceptable noise exposures near major urban airfields. This enabled making the Federal Aviation Rule, which set maximum takeoff, landing and sideline noise levels for certification of new turbofan powered aircraft. In 1990, Congress promulgated the Airport Noise and Capacity, ordering the FAA, Federal Aviation Authority, to set noise limits. The resulting Federal Aviation Regulations, FAR Part36, mandated noise reductions for civil aircraft weighing more than $75,000$ *lb* [1]. These limitations made every authority make their own certification; AP36 Russia, CS36 EASA, JAR36 JAA, FAR Part 36 USA, ICAO Annex 36, Figure 1.6.

Because of these restrictions, airport noise is now a major design criterion for civil aircraft. So, an understanding of the mechanism of noise production and of the technique for alleviating it is crucial for aircraft propulsion research and development. The new performance criterion, aeroacoustics, became mainly a research area after 1960s. This can be seen as shown in Figure 1.7. Over a half century period, a decrease of 20 *dB* achieved. This is a sign of success about one tenth pressure fluctuation decrease.

The comparison between noise measurements is done with a universal scale, decibel (*dB*). The decibel, *dB*, is a measure, on a logarithmic scale, of the magnitude of the sound pressure with respect to a standardized reference quantity. Sound Pressure Level, *SPL*, is calculated as follows;

$$SPL = 20 \log_{10} \frac{P}{P_{ref}} [dB] \tag{1.1}$$

where $P_{ref} = 20 \times 10^{-6}$ *Pa*.Dynamic levels of sound range from about 0 *dB* (threshold of audibility) to about 120 *dB* (threshold of pain). The range of frequencies perceived by the human ear is only 20 *Hz* - 20000 *Hz*. However, the ear is much more sensitive in the 2-4 *KHz* range. Approximately, 5 *dB* differences can be realized by humans.

The use of acoustic absorber liners in the air and gas flow ducting of a power-plant has made a significant contribution to noise reduction. Liners function in two basic ways: resistive and reactive. In a resistive liner, sound energy is dissipated by the physical damping of sound pressure. In a reactive liner, incident and reflected rays are used to cancel each other and so reduce the total noise energy. The first of these tends to be more useful because it covers a broader frequency range [26]. The absorbing material is divided into small compartments which

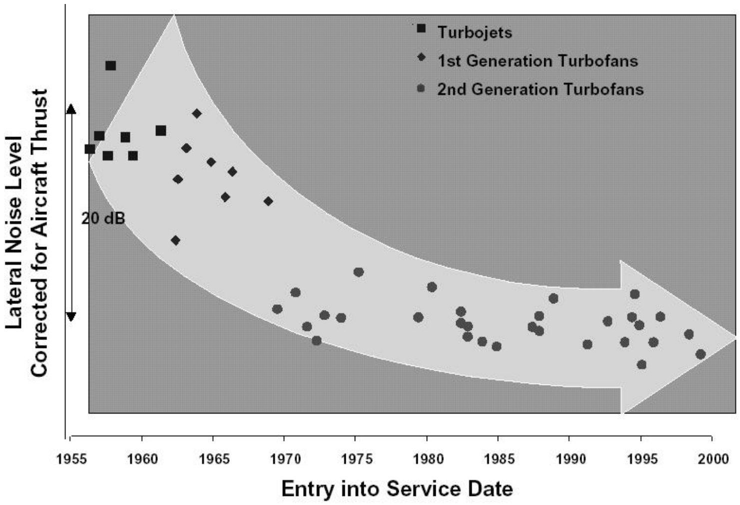

Figure 1.7: The overall noise level decrement over the years [6].

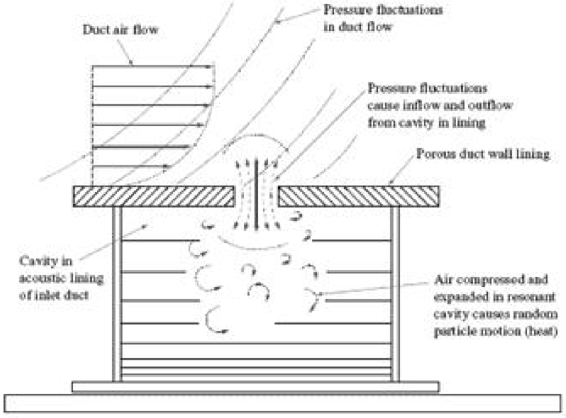

Figure 1.8: Attenuation with liners [56].

are small relative to the wavelength of sound, as in Figure 1.8. Multiple degree of freedom, two layer or more, liners are used too. The performance of a locally reacting liner is defined by its impedance, which is expressed as follows:

$$Z(\omega) = R(\omega) + iX(\omega) \tag{1.2}$$

Two performance parameters are resistance and reactance. The resistance, R, determines the peak level of attenuation. The reactance, X, determines both the frequency at which attenuations peak dependent on the dept of core and the bandwidth of attenuation facing sheet reactance. The normalized acoustic impedance, Z, relates the acoustic pressure, p, and the particle velocity, v, normal to the liner surface, so that;

$$p = Z\rho_0 a_0 v \tag{1.3}$$

In physical aspect, sound waves exhibit reflection, difraction, refraction, dispersion, dissipation characteristics. The reflection of sound follows the law "angle of incidence equals angle of reflection", sometimes called the law of reflection. The reflected waves can interfere with incident waves, producing patterns of constructive and destructive interference. This can lead to resonances called standing waves in rooms. It also means that the sound intensity near a hard surface is enhanced because the reflected wave adds to the incident wave, giving pressure amplitude that is twice as great in a thin "pressure zone" near the surface. This is used in pressure zone microphones to increase sensitivity. The doubling of pressure gives a 6 dB increase in the signal picked up by the microphone. Reflection of waves in strings and air columns are essential to the production of resonant standing waves in those systems. So reflection from the boundary acts such that sound waves coming to hard wall change its polarity with conserving their speed and amplitude. The ones coming to soft wall reflect by conserving amplitude, speed and polarity.

Diffraction is the bending of waves around small obstacles compared to wavelength and the spreading out of waves beyond small openings. The fact that you can hear sounds around corners and around barriers involves both diffraction and reflection of sound. Diffraction in such cases helps the sound to "bend around" the obstacles, such as duct lip. The fact that diffraction is more pronounced with longer wavelengths implies that you can hear low frequencies around obstacles better than high frequencies. Another implication of diffraction is the fact that a wave which is much longer than the size of an obstacle cannot give you information about that obstacle.

Refraction is the bending of waves when they enter a medium where their speed is different. Bending of sound waves does occur and is an interesting phenomenon in sound. These visualizations may help in understanding the nature of refraction. A column of troops approaching a medium where their speed is slower will turn toward the right because the right side of the column hits the slow medium first and is therefore slowed down. The marchers on the left, perhaps oblivious to the plight of their companions, continue to march ahead full speed until they hit the slow medium. Not only does the direction of march change, the separation of the marchers is decreased. When applied to waves, this implies that the direction of propagation of the wave is deflected toward the right and that the wavelength of the wave is decreased. From the basic wave relationship, $v = f\lambda$, it is clear that a slower speed must shorten the wavelength since the frequency of the wave is determined by its source and does not change. Another visualization of refraction can come from the steering of various types of tractors, construction equipment, tanks and other tracked vehicle. If you apply the right brake, the vehicle turns right because you have slowed down one side of the vehicle without slowing down the other.

In addition to these, numerical dissipation and dispersion are the basic factors that affect the sound radiation. Dissipation is roughly speaking, numerically-induced energy loss. The solution will eventually be different in amplitude and phase to the approximation solution provided by a scheme with less dissipation. The phase phenomenon must be considered too, since the scheme will in general have different rates of dissipation for different modes. Dispersion is the type of error by which the computed solution will gradually get out of phase with the exact solution.

Rarefaction is a part of a sound wave where the pressure is less than the atmospheric pressure, the opposite of compression. The displacement of air particles within a cycle involves alternations of compressions and rarefactions to produce sound.

1.2 Aeroacoustics

Aeroacoustic phenomenon includes two basic mechanism; generation and propagation in a medium. In an acoustic measurements, Fourier transformation of time history of a sound content gives it in frequency spectrum. In the spectrum, broadband noise and discrete noise contents which are main objectives in aeroacoustics are observed. Broadband noise is generated by propellers, rotors and airframes. Broadband noise is related to random processes which result from the interaction of turbulent flow fluctuations with rotor blades and stator vanes. These fluctuations can be in the form of turbulent boundary layer on blades/vanes and vortex shedding from them, and turbulence in the incident airstream. Even though it is often the dominant noise around 3 *kHz* where human ears are more sensitive, it is not seen as important as other noise sources. This is primarily because of research's focus on propellers and rotors where discrete noise are 10-30 *dB* higher than the broadband noise levels[22, 27]. Nonetheless, as progress has been made in minimizing other noise sources, it is becoming more important to reduce broadband noise. The discrete-frequency noise is generated by a rotor-stator interaction. Discrete-frequency tones are generated by periodic interactions between rotating and non-rotating blade rows. Namely, the fan exit guide vane is subject to the potential field and viscous wake of the fan rotor. The impact of the rotor potential field is releaved by maximizing the axial spacing between the fan rotor and the exit guide vane. Potential flow interactions can become of concern if the axial spacing between blade rows is small or the flow Mach number is high. The viscous wake of the rotor persists over considerable axial distances, and is the primary source of excitation seen by the exit guide vane. The fan exit guide vane operates in an extremely complex flow field generated by highly loaded, arbitrarily shaped airfoils. These complexities change the convection characteristics of the gust and make calculation of the generated noise difficult. Experimental studies showed that any reduction in tonal noise results in a reduction in broadband noise [11].

All noise in the flow is a reflection of unsteadiness in the flow. The fluctuating terms are usually smaller of magnitude than the mean state quantities. An acoustic disturbance is about 10^{-5} of mean state quantities [28]. Acoustic energy is the potential distortion that the corresponding acoustic sources have. As reported anecdotically by Ffowcs-Williams and Crighton, it has been calculated that the first generation of Boeing 707 at take-off produced as much sound as the world population shouting in phase together. A Boeing 767 of 30 years later (with four times as much thrust per engine) produced as much sound as the city of New York shouting in phase. However, the energy radiated by such sound in the first 45 seconds is just enough to cook one egg [4]. "jet noise" and "sound generated aerodynamically" were preferred titles around 1960s. Around 1970s, "aeroacoustic" was adopted as the descriptive title for all aspects of interactions that take place between sound and flow. The pioneering aeroacoustic studies could only start with pioneers. Lord Rayleigh's works in the area of physics are important foundations. His success in combining natural phenomena and physical basics behind them constituted aerodynamic sound. His study in inhomogeneous wave equation with the assumption of nonuniformity of stationary acoustic medium being due to density and compressibility is reviewed with the assumption of turbulent velocity perturbations by Lighthill [29]. The developed aeroacoustic theoretical knowledge with Lighthill's paper shed light on 1960's aeroacoustic studies. This masterpiece enabled the use of mathematical knowledge on aerodynamic noise generation with the flow variables. Thus, the quadruple terms in his theory would yield a scaled effect of eight power of jet velocity (U^8) [18]. Missing parts in Lighthill's theory are focused and important results are obtained through the preceding century. All of these formed today's computational and experimental aeroacoustic basics [3].

All numerical methods need supporting backgrounds such as experimental or analytical approaches to understand how the applied method is effective. Experimental studies in aeroacoustics are very expensive facilities as in the case of experimental aerodynamics. The evaluation of static and in-flight data is a severe problem. Measurements obtained from ground static tests are not representative of the noise measured in flight tests due to installation effects, flight effects, atmosphere and ground effects. It is also found that several mechanisms are involved in the noise generation process and one mechanism may dominate under one test condition while another mechanism dominates during a different flight test. Test section is to require anechoic tunnels insulated against external sources and sensitive instruments able to measure especially the high-frequency pressure fluctuations. Besides, this instrumentation has to be coupled with flow visualization techniques in order to understand the relationship between aerodynamics and acoustics [9, 10, 14, 17, 25].

Computational acoustics , *CAA*, is a tool that can not be given up for acoustic radiation problems. CAA is suggested gradually as an applicable tool for detailed analysis of engineering problems in which noise plays a significant role. The problems involving noise generation and propagation in a number of problems of interest like jets, cavity flows, and duct radiation [24, 15, 16]. The promise of CAA has considerable ability to simulate accurately the physical processes involved in the generation and propagation of sound. Thus, it can match the knowledge obtained from analytical and experimental methods. Its significance as a major contributor to the total noise output of a modern aero-engine and the need to mitigate noise emissions from aircraft for environmental reasons drives the reason for understanding and estimating fan noise derives [21].

Due to the complexity, CAA may be used in tackling some outstanding issues in fan noise modelling. The aeroacoustics of high bypass ratio turbofan engines necessitates a detailed analysis of the turbomachinery self-systems, impact of the fluctuating pressure patterns on aerodynamic surfaces, transmission of the resultant modes in the inlet/exhaust ducts, interaction of the dominant modes with the liner material, and the prediction of farfield noise. To devise effective means of reducing fan noise, a detailed understanding of its mechanisms and characteristics is required [22]. Many of the current theoretical models used in fan noise prediction rely on simplified descriptions of the hardware and flow conditions that are present inside the engine. Consequently, such models do not have the required reliability to describe all of the relevant physical mechanisms involved in the generation of fan noise. They are a reflection of limited use for developing effective noise mitigation methods [23]. Experimental approaches have also seen only limited success in tackling the fan noise problem. The overlapping nature of its sources which often mask the contribution from a specific source under consideration and the dependence of strengths of various sources of fan noise on the fan rotational speed, which can vary significantly with the engine power setting, are other difficulties encountered [27].

In view of these, CAA can provide reasonable help in handling of the fan noise modelling procedure. Depending on the focused problem, this help can be in the form of fundamental theoretical studies to uncover mechanisms involved in noise generation.

1.3 Numerical Studies on Fan Noise

Fan noise is associated with the fan stage of a turbofan aeroengine and is produced by a number of different sources. Most of the acoustic sources involve the interaction of small unsteady flow perturbations, vortical and acoustic, with the fan rotor and stationary guide vane blade rows within the stage [11, 12, 13]. These are mainly interaction of inflow distortions and the inlet boundary layer with the fan and the interaction of fan flow perturbations with the bypass and core stators, such as blade viscous wakes, tip clearance flow. Another type of interaction can also be self-generated, self-noise, as in the case of the noise produced by scattering of blade boundary layer turbulence at the blade trailing edge, local separation of the flow on the airfoil, noise associated with vortex shedding at the trailing edge. Depending on the nature of the unsteady perturbations involved, the interaction sources generate discrete frequency tones or broadband noise or both. Other sources associated with the steady part of the flow within the fan stage include the interaction of the fan with the steady pressure field of the engine struts and the Multiple Pure Tones (MPT) of the fan, buzz-saw noise, that are produced as a result of spatial non-uniformities in the rotor-locked pressure field. The fan-strut interaction produces discrete tones at the harmonics of the blade passing frequency, while buzz-saw is produced at the multiples of fan shaft rotational frequency.

When a rotating machine is mounted in a duct, the flow it produces is not, of course, the same as in free-space. This modification of the aerodynamic behavior of the machine affects the blade loadings, then the noise sources. But this is as aerodynamic point. On the acoustic point of view, the duct strongly modifies also the propagation from the sources. More precisely, the effects of the duct are twofold: the duct causes a re-organization of the natural acoustic field of the sources by reflections on the walls, and produces special guided vanes, these waves radiate outside in the farfield through the duct termination, thanks to a complicated diffraction process. Whether these effects are important or not depends on the compared values of the acoustic wave length and the length of the duct. Generally speaking, when the duct is very short, in the sense that the dimensions are small in comparison with the wave length, it can be neglected without significant error. When it is long, the two proceeding effects are certainly important but they can be separately taken into account by analytical methods.

Most of the computational analysis performed in the area of high bypass ratio engine acoustics fall into two broad characteristics: Direct time domain approaches have become popular and most of the methods in this group are a result of the maturation of computational fluid dynamic algorithms that can be applied to aeroacoustic problems. The main advantages of time domain methods is the ability to handle multifrequency sources in one single simulation. However the main drawback of time-domain methods relates to treatment of frequency-dependent lining material. The other methods, frequency-domain methods, that represent a second class of noise prediction methods for aircraft engines. While frequency domain methods are not as efficient as the time domain methods for broadband noise predictions, and are cumbersome to use for multifrequency noise sources, they provide important insight into the functioning of liner materials that are generally tuned to resonate at a single frequency or a narrow band of discrete frequencies. Furthermore, the use of frequency-domain methods eliminates questions about the accurate resolution of temporal characteristics associated with the prediction algorithm.

The first step in determining how to solve the sound generation problem in a flow is to look for applicable assumptions applicable to the flow without losing generation and propagation characteristics. The dominant mechanisms should be captured. The next step is to apply the prescribed method to the problem with a numerically well detailed computational approach. Numerical approach have to accomplish some challenges that arise because acoustic waves are very weak compared to near-field fluctuations, and because they must propagate with little attenuation over long distances. In fact this has necessitated the use of high order-accurate numerical methods, and in particular compact and optimized finite difference and Runge-Kutta time marching schemes, and boundary conditions being the other part of the errors. Dissipation and dispersion errors are also numerical attenuation problems. Also low Mach number problems can have some numerical errors that overestimates the sound. Efficient and accurate solutions can be obtained by using high order and optimized finite difference schemes due to the requirement of preserving the shape and frequency of wave propagation and generation. In acoustic problems, a consistent, stable and convergent high order scheme doesn't guarantee a good numerical solution, either. Tam and Webb [30] developed an optimized high order finite difference scheme which is applicable for wave propagation with a low dispersion. Dispersion Relation Preserving, *DRP*, Scheme optimized with Fourier Transform of Taylor series expansions is a way to capture the acoustic disturbance propagation with low dispersion. This method further developed as compact finite difference schemes by Kim and Lee [31] with an introduction of weighting function for maximum spatial resolution. Time integration is as important in preserving accurate wave propagation characteristics as is the choice of spatial discretization. Classical time integration schemes can introduce dispersion and dissipation into solution. Runge-Kutta schemes are the most commonly used type of time advancing schemes in CAA. Hu et al. [31] established a p-stage LDDRK at which each stage has optimized coefficients by minimizing a specific integral. One of the most challenging aspects of CAA is the imposition of stable and accurate boundary conditions. These boundary conditions in addition to their physical responsibilities must satisfy no reflection from the boundary into the domain. The physical domain can be surrounded by inflow, outflow, radiation, wall and impedance boundaries. Giles [32] established a characteristics-based inflow boundary condition with a reasonable nonreflection. Bayliss and Turkel [33] aimed an asymptotic solution type radiation boundary condition allowing radiation of energy out of domain, accurate application for constricted domain and acceleration through steady state. Also Tam and Webb [30] presented a set of radiation and outflow boundary conditions which are compatible with the proposed high order finite difference schemes. Reflection problem in acoustic propagations revealed application of buffer zone techniques and Perfectly Match Layer (PML) techniques. Hu [53] developed PML equations for Euler equations. In this approach, PML equations are solved in an added region to the boundary so that the out-going waves are absorbed inside the layer with little reflection to the interior domain. By the way, to avoid generating instability waves in the PML domain, it has been found necessary to introduce a coordinate transformation before applying the PML technique [53]. Buffer zone for inflow boundaries in a duct afforded as an explicit damping by Zhang et al. [34]. This zone absorbs the reflected waves through in the duct and works as a matching zone. Rigid solid boundaries are represented by the no-slip condition, which specifies that there is no relative motion between the fluid and solid. Thompson [35] suggests an extrapolation procedure based on a one-dimensional analysis of the acoustic reflection problem at the interface, imposing rigidity of the boundary by perfect reflection of waves with normal incidence. Besides, appropriate to the Euler equations fluid particles are free to slip at a hard wall under pressure fluctuations' influence, by setting normal component contravariant velocity to zero, getting tangential, azimuthal contravariant velocity and pressure with the help of extrapolation. Myers [36] derived a general form of the frequency-domain impedance condition assuming that a soft wall undergoes small deformations about a mean stationary surface in response to an incident acoustic field from the fluid about a mean flow. Impedance boundary conditions became applicable to time-domain approaches with the study of Özyörük and Long [37]. This study provided broadband noise calculations in time-domain. With numerical solutions of the NASA Langley Research Center flow impedance tube, this form of an impedance boundary condition coupled with Euler/Navier Stokes type solvers, can adequately simulate the effects of liner materials in engine inlet and exhaust ducts .

The noise generating mechanisms in turbofan engines have been investigated and classified by Tyler and Sofrin [13]. It has been showed that pressure field produced by the compressor consists of spinning modes. Also pressure pattern speed in duct is a determining factor for propagation of these modes.

Ray acoustics method is used for acoustic pressure calculations by Doughherty [43]. FEM , finite element method, is applied generally for low frequency range than that of Ray acoustics, where Ray acoustics captures the dominant SPL ranges. But, with the help of high frequency approximation Ray acoustics disregard interference effects.

Eversman [23] described a FEM (Finite Element Method) predicting the near and far field acoustic radiation from the aft fan duct of a turbofan engine. The shear layer modelling is used in this potential flow code as a separation boundary condition for two independent potential regions. The obtained results captured refraction effect in this shear layer well.

Özyörük, and Long [41] applied a multigrid method with a fourth-order accurate finite difference Runge-Kutta time marching scheme for nonlinear Euler equation for efficient noise radiation from engine inlets. Convergence acceleration multigrid method that retains the high-order accuracy of a typical, explicit, high-resolution CAA algorithm is presented.

Özyörük, Ahuja and Long [40] investigated the radiation problem from the engine inlets with the aid of numerical simulations of the Euler/Navier-Stokes equations coupled with a time-domain methodology that analyzes the impedance characteristics of liner materials. This method with multigrid approach procure a steady solution that represents the underlying mean flow, and analytically specify the noise generating mechanisms as part of boundary condition procedure in the unsteady simulations.

Zhang et al. [34] solved duct propagation problem from a bypass duct with LEE. In this study the radiation of sound waves from a by-pass duct with matching of MS and CAA calculations showed a good propagation characteristic, like diffraction at the lip and nonlinear multi cut-on mode radiation peak effect.

Özyörük and Long [39] performed a time-domain method through a combination of Euler and linearized Euler solver, coupled with Kirchhoff formulation for farfield prediction. The focus on this paper is on fan noise and not on jet noise. Both inlet and aft duct propagation with acoustically treated boundaries are examined. The numerical approach at the aft section is LEE due to difficulties in exhaust fan-face boundary conditions and the appearance of shear layer instabilities in full Euler solution.

Özyörük et al. [38] afforded a frequency-domain approach for inlet duct noise radiation with LEE in frequency domain by nonuniform background flow and acoustic treatment conditions. The temporal integration is captured by an explicit pseudo-time marching technique, which allows efficient solutions of LEE on parallel computers. Due to its explicit expression, it has convergence acceleration property.

Long [42] described a new way to write and solve the governing equations of fluid dynamics that is very well suited to aeroacoustics problems. The flow variables are splitted into mean and fluctuating parts, using the nonconservative equations. Results treated a good propagation characteristic in engine duct.

X. Zhang et al [50] studied on the prediction of higher order spinning mode radiation from an unflanged duct, with and without mean flow with linearized Euler equation in time domain. In the study, the applied method agreed with the analytical solution. The radiation pattern mesh is stretched according to some predetermined PPW, point per wavelength, values in and around the duct. So, the obtained results are less sensitive to mesh characteristics. The comparison of the result with this time domain method is summarized in results section.

Philbrick and Topol [44] applied a rotor/stator wake interaction code for tonal source modelling. An accurate wake model is described as a function of fan geometry and operating conditions by defined correlation factors for complex mode amplitude prediction.

Glegg and Jochault [45] described a self noise prediction due to blade boundary layer turbulence with blade trailing edge, trailing edge noise. This study gives a first order estimate of the trailing edge noise from a ducted fan.

Parrett and Eversman [46] developed a method of wave envelope elements relying on the assumption of some distance from the inlet sound field approximates that produced by a point source and makes feasible a numerical solution of the acoustical radiation problem.

Benzakein [11] researches on Fan Noise characterized the generation and propagation of MPT, in the view of Rotor/stator spacing, Vane/blade ratio effects. The general idea about that MPT propagates only when rotor tip number is greater than 1 is reviewed as although they are formed below that critical velocity they propagate above this limit.

Dunne and Howe [46] worked on a simplified analytical approach for the sound generation from blade-vortex interaction.

Nallasamy and Envia [48] designed a CFD based, RANS, method for the prediction of inlet and exhaust broadband noise sound radiation from the rotor wake turbulence stator interaction.

For farfield predictions, there are mainly two types of approach; Kirchhoff and Ffowcs-Williams formulations. Two methods have different approaches to calculate the farfield directivity. Both method eliminates the huge calculation time and mesh requirements for numerical approaches at farfield. The main difference between the methods is that input to the applied integrals are different in nature. Disadvantages of the Kirchhoff method are to require the normal derivative of pressure which can be difficult to calculate in some aerodynamic problems and to choose the control surface in the linear flow region since it does not include nonlinear flow effects. Because Kirchhoff formulation is a type of wave equation , the selection of the linear region for the method is a problem dependent. Inspite of this, the FW-H formulation is constructed on the conservation laws of fluid mechanics. Nonlinearities within its quadrupole term enables that the integration surface can be placed in the nonlinear regions of the flow field.

Brentner and Farassat [51] showed that neglected quadrupole term in the FW-H solution makes it less sensitive than the Kirchhoff method to the placement of integration surface. The main disadvantage of the FW-H method is that the quadrupole source term must be included for problems involving high speed flows. Brentner and Farassat [51] pointed that if the position of integration surface is chosen such that it in linear flow region, the FW-H formulation behaves like the Kirchhoff formulation. The quadrupole term is a volume source. So, volume integration is computationally expensive and can be difficult to evaluate. Some approximations relieve the computational load for this volume source.

1.4 Thesis Scope and Outline

This study aimed to develop a frequency-domain code that includes the effects of non-uniform background flows and acoustic treatments by iterative approach. This code has the method of the linearization of the Euler equations about a mean flow that comes from CFD solutions, so that its effects on sound propagation are included in computations more realistically. Parallelization methodology of distributed memory architectures with domain decomposition and the Message Passing Interface (MPI) for inter-processor communications applied. Solution domain is divided into subdomains of nearly equal grid point load. It would be particularly important for aft radiation from turbofans that the shear layer emanating from the shroud of the engine may cause significant rarefaction of the emitted sound waves. Today, either experimental or 3-D numerical direct methods are so difficult to handle. Experimental methods as stated in preceding paragraphs are very expensive and difficult to build up the test section. Their calibration requirement is a considerable drawback. Frequency domain approach applied as an iterative approach with pseudo time derivative term addition to general equations. Although their convergence characteristics are better, the direct methods cause such huge solution time and matrix, sparse matrixes. This summarizes that direct methods are more expensive than iterative type solutions. An ongoing study by Prof. Yusuf Özyörük includes this part of application in frequency domain for propagation of sound. Some results are compared with this direct method case in Chapter 3.

Chapter 2 is about Numerical Method applied through this study. In the chapter, equational form of the applied methodology illustrated in frequency domain equations. Applied buffer zone technique also included in the chapter with an improved version of previously used explicit damping type.

Chapter 3 includes solutions of the applied methodology for some cases. From point of propagation of sound, some computational examples are chosen for some specific modes. Solutions includes the effect of background flow, buffer zone and characteristic based boundary conditions to radiation of the acoustic modes with Runge-Kutta type time integration. Numerical method in this study uses buffer case as a damping boundary conditions for spurious waves in the duct. Effect of frequency or cut-off ratio to buffer zone is illustrated with some supporting solutions. The results are compared with direct method in frequency domain. Farfield results are obtained by Kirchhoff method on a predetermined surface mesh. The selection criteria of Kirchhoff surface is summarized with selection of different Kirchhoff surfaces for the same case. And, some farfield results are illustrated. The generated code is based on aft duct radiation. The effect of shear layer to farfield and propagation pattern is also analyzed.

Discussion and Conclusion section includes investigations of the results obtained. From physical and numerical aspect, they are discussed and concluded about buffer zone technique with the effect of mean flow and acoustic field. Through these comparisons, farfield directivity computed by the present approach and direct method results are taken as basic.

CHAPTER 2

NUMERICAL METHOD

2.1 Introduction

In this chapter, the numerical method employed to compute the frequency domain prediction of turbofan noise is summarized. First, the mean flow is computed for steady state flow variables and shear layer with the linearized Euler equation (LEE). Obtained background flow is sent to frequency domain code. The full domain is divided into sub-zones. The computations on each sub-zone are performed in parallel. MPI message passing library routines are used in the parallel solution algorithm. The computed noise patterns are analyzed in terms of mean flow effect, reflection, diffraction, refraction and rarefaction, acoustically treated material effects, radiation pattern, buffer zone success.

2.2 Governing Equations

2.2.1 Linearized Euler Equation

The iterative finite difference formulation of Euler equation is solved on a computational domain, including several sub-zones. In the near field in and around duct exit, we model the noise propagation through solutions of the linearized Euler Equation (LEE). LEE admits entropic, vortical and acoustic disturbances with non-uniform mean flows. Each sub-zone has a rectangular grid and the distribution in each are arranged such that the solution time in each zone is nearly same. Linearized equations are given in cylindrical co-ordinates by,

$$\begin{aligned}
&\frac{\partial \rho'}{\partial t} + \rho_0(\frac{\partial u'}{\partial x} + \frac{\partial v'}{\partial r} + \frac{v'}{r} + \frac{1}{r}\frac{\partial w'}{\partial \theta}) + u_0\frac{\partial \rho'}{\partial x} + v_0(\frac{\partial \rho'}{\partial r} + \frac{\rho'}{r}) + \rho'(\frac{\partial u_0}{\partial x} + \frac{\partial v_0}{\partial r}) + u'\frac{\partial \rho_0}{\partial x} + v'\frac{\partial \rho_0}{\partial r} = 0\\
&\frac{\partial u'}{\partial t} + u_0\frac{\partial u'}{\partial x} + v_0\frac{\partial u'}{\partial r} + u'\frac{\partial u_0}{\partial x} + v'\frac{\partial u_0}{\partial r} + \frac{1}{\rho_0}\frac{\partial p'}{\partial x} = 0\\
&\frac{\partial v'}{\partial t} + u_0\frac{\partial v'}{\partial x} + v_0\frac{\partial v'}{\partial r} + u'\frac{\partial v_0}{\partial x} + v'\frac{\partial v_0}{\partial r} + \frac{1}{\rho_0}\frac{\partial p'}{\partial x} = 0\\
&\frac{\partial w'}{\partial t} + u_0\frac{\partial w'}{\partial x} + v_0\frac{\partial w'}{\partial r} + \frac{1}{\rho_0 r}\frac{\partial p'}{\partial \theta} + \frac{v_0 w'}{r} = 0\\
&\frac{\partial p'}{\partial t} + u_0\frac{\partial p'}{\partial x} + v_0\frac{\partial w'}{\partial r} + u'\frac{\partial p_0}{\partial x} + v'\frac{\partial p_0}{\partial r} + \gamma p_0(\frac{\partial u'}{\partial x} + \frac{\partial v'}{\partial r} + \frac{v'}{r} + \frac{1}{r}\frac{\partial u'}{\partial \theta}) + \gamma p'(\frac{\partial u_0}{\partial r} + \frac{\partial v_0}{\partial r} + \frac{v_0}{r}) = 0
\end{aligned} \tag{2.1}$$

The 3-D, time domain, LEE equations are transformed into the frequency domain assuming that perturbations of the primitive-dependent variables of the form;

$$Q'(x,t) = \Re[\widehat{Q}(x,r,\omega)e^{i\omega t + im\theta}] \tag{2.2}$$

where,

$$\begin{aligned}
Q' &= [\rho', u', v', w', p']^T\\
\widehat{Q} &= [\widehat{\rho}, \widehat{u}, \widehat{v}, \widehat{w}, \widehat{p}]^T
\end{aligned} \tag{2.3}$$

And $i = \sqrt{-1}$; ρ',u',v',w',p' are density and the velocity perturbations, the pressure ,respectively, in the cylindrical (x,r,θ) coordinate directions. A hat on the variable indicates a complex quantity. In Equation 2.2, ω is the circular frequency and integer m represents the azimuthal mode number.

Substitution of Equation 2.2 into the linearized Euler equations, Equation 2.1, in cylindrical co-ordinates the equations governing the complex amplitudes of the flow perturbations become,

$$\begin{aligned}
&i\omega\widehat{\rho} + \rho_0\frac{\partial \widehat{v}}{\partial r} + \widehat{v}\frac{\partial \rho_0}{\partial r} + v_0\frac{\partial \widehat{v}}{\partial r} + \widehat{\rho}\frac{\partial v_0}{\partial r} + \frac{1}{r}(\rho_0\widehat{v} + v_0\widehat{\rho}) + \rho_0\frac{\partial \widehat{u}}{\partial x} + \widehat{u}\frac{\partial \rho_0}{\partial x} + u_0\frac{\partial \widehat{\rho}}{\partial x} + \widehat{\rho}\frac{\partial u_0}{\partial x} + \rho_0\frac{im}{r}\widehat{w} = 0\\
&i\omega\widehat{u} + u_0\frac{\partial \widehat{u}}{\partial x} + v_0\frac{\partial \widehat{u}}{\partial r} + \widehat{u}\frac{\partial u_0}{\partial x} + \widehat{v}\frac{\partial u_0}{\partial r} + \frac{1}{\rho_0}\frac{\partial \widehat{p}}{\partial x} = 0\\
&i\omega\widehat{v} + u_0\frac{\partial \widehat{v}}{\partial x} + v_0\frac{\partial \widehat{v}}{\partial r} + \widehat{u}\frac{\partial v_0}{\partial x} + \widehat{v}\frac{\partial v_0}{\partial r} + \frac{1}{\rho_0}\frac{\partial \widehat{p}}{\partial r} = 0\\
&i\omega\widehat{w} + u_0\frac{\partial \widehat{w}}{\partial x} + v_0\frac{\partial \widehat{w}}{\partial r} + \frac{im}{\rho_0 r}\widehat{p} + \frac{v_0\widehat{w}}{r} = 0\\
&i\omega\widehat{p} + u_0\frac{\partial \widehat{p}}{\partial x} + v_0\frac{\partial \widehat{p}}{\partial r} + \widehat{u}\frac{\partial p_0}{\partial x} + \widehat{v}\frac{\partial p_0}{\partial r} + \gamma p_0(\frac{\partial \widehat{u}}{\partial x} + \frac{\partial \widehat{v}}{\partial r} + \frac{\widehat{v}}{r} + \frac{im}{r}\widehat{w}) + \gamma\widehat{p}(\frac{\partial u_0}{\partial x} + \frac{\partial v_0}{\partial r} + \frac{v_0}{r}) = 0
\end{aligned} \tag{2.4}$$

where $[\rho_0, u_0, v_0, 0, p_0]^T$ represent the non-uniform, axisymmetric, mean flow variables. Looking at Equation 2.1 and Equation 2.4, it can be seen that the latter one contains derivatives only in (x,r). This difference results from azimuthal variations transformed to the terms multiplied by *im*. So frequency domain LEE has less gradient variables to compute, this reduces the computational expense of full 3-D.

2.3 Boundary Conditions

In numerical simulations of problems, a set of equations is required to model boundary conditions. These boundary conditions are applied all around the interior computational domain where the flow equations are solved. While applying boundary conditions, the physics of a particular problem must be modelled correctly by required mathematical expressions. For some particular problems, additional numerical boundary conditions may be required. The manner in which boundary conditions are specified must be considered in the overall stability and accuracy of numerical scheme used to solve the system. The boundary conditions can be applied explicitly or implicitly. They must allow the flow disturbances to leave the computational domain without significant reflections. This is crucial in computational aeroacoustic (CAA), since spurious acoustic waves generated by poor boundary condition application may mask the physical sound field radiated. The applied boundary conditions are summarized in the following paragraphs.

2.3.1 Fan-Face condition

2.3.1.1 Acoustic source conditions

In order to excite the acoustic field, exact cylindrical duct eigensolutions are used at the fan face which is assumed to be a deviation from the mean field. To obtain the following equation, wave equation is written in cylindrical coordinates and with help separation of variables technique general solution in terms of Bessel equations is obtained. Acoustic pressure in hard-walled duct at a constant x plane for a circular annular duct is given by,

$$\widehat{p}(r,\theta) = \sum_{m,\mu} A_{m,\mu}[J_m(k_{m,\mu}r) + Q_{m,\mu}Y_m(k_{m,\mu}r)]e^{i(m\theta)} \tag{2.5}$$

where m and μ are the azimuthal and radial mode orders, respectively; $A_{m,\mu}$ is the amplitude of (m,μ) mode; J_m and Y_m are the m^{th} order Bessel functions of the first and second kinds, respectively; $k_{m,\mu}$ are the eigenvalues that make the transcendental equation zero resulting from the wall condition, $\frac{\partial p}{\partial r}|_{wall} = 0$; $A_{m,\mu} = -J'_{m,\mu}(\sigma k_{m,\mu})/Y'_{m,\mu}(\sigma k_{m,\mu})$ in which a prime indicates a derivative with respect to r, and σ is the hub to tip ratio. When there is no center body $Q_{m,\mu}$ is zero. The azimuthal mode order m is found using the rotor stator interaction theory of Taylor and Sofrin [13]. In this theory, the circumferential mode order m is obtained by,

$$m = nB + sV \tag{2.6}$$

where B and V are the number of rotor blades and stator vanes, respectively, n is the time harmonic index and s is any integer number. Once the number of rotor blades, the number of exit guide vanes and the rotor speed are known, the modes that are cut on are determined based on the local mean flow conditions at the source plane, which is usually taken as the fan face. Outflow boundary conditions are applied at the source plane conjunction with Equation above. The non-reflecting boundary conditions of Giles [32] are adapted to the present work to introduce the incident acoustic waves into the domain while letting outgoing ones leave it with minimal reflection. The adopted conditions are given in the frequency domain by,

$$\begin{aligned}
&i\omega\widehat{u} + \tfrac{u_0+c_0}{2\rho_0 c_0}\left(\tfrac{\partial\widehat{p}}{\partial x} + \rho_0 c_0\tfrac{\partial\widehat{u}}{\partial x}\right) + \tfrac{(c_0-u_0)}{4}\left(\tfrac{\partial\widehat{v}}{\partial r} + \tfrac{\widehat{v}}{r} + \tfrac{im}{r}\widehat{w}\right) = i\omega\tfrac{L_1}{\rho_0 c_0}\\
&i\omega\widehat{v} + u_0\tfrac{\partial\widehat{v}}{\partial x} + \tfrac{1}{\rho_0}\tfrac{\partial\widehat{p}}{\partial r} = 0\\
&i\omega\widehat{w} + u_0\tfrac{\partial\widehat{w}}{\partial x} + \tfrac{im}{\rho_0 r}\widehat{p} = 0\\
&i\omega\widehat{p} + \tfrac{u_0+c_0}{2}\left(\tfrac{\partial\widehat{p}}{\partial x} + \rho_0 c_0\tfrac{\partial\widehat{u}}{\partial x}\right) + \tfrac{3c_0+u_0}{4}\left(\tfrac{\partial\widehat{v}}{\partial r} + \tfrac{\widehat{v}}{r} + \tfrac{im}{r}\widehat{w}\right) = -i\omega L_1
\end{aligned} \tag{2.7}$$

where L_1 is set to the incident part of the acoustic pressure that is given by equation 2.5. Numerical experimentation has shown that these conditions do not completely eliminate the outgoing waves [38]. The radial wave number is determined from turning points of the Bessel function, and axial wave number and cut-off ratio are calculated from Equation 2.8 and

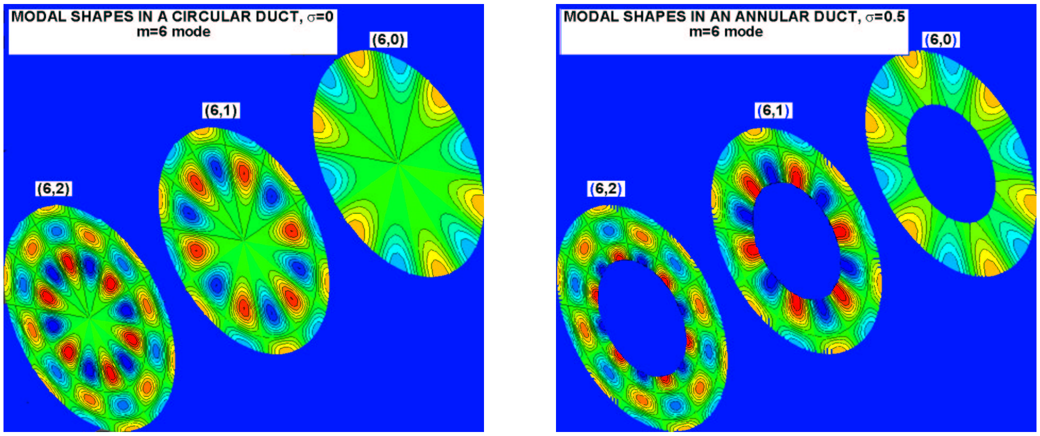

(a) Circular Duct Mode pattern.

(b) Annular Duct Mode pattern.

Figure 2.1: Circular and Annular Duct Mode pattern for $m = 6$.

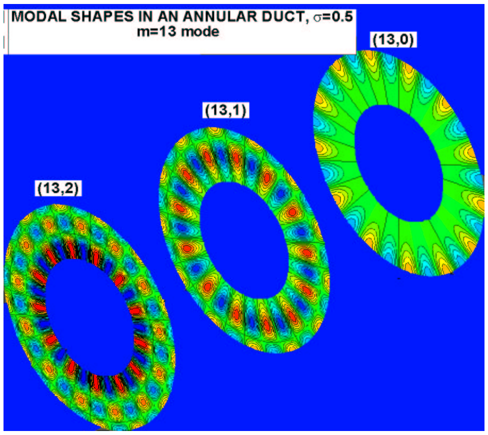

Figure 2.2: Annular Duct Mode pattern for $m = 13$.

Equation 2.9 respectively.

$$k_a = (k/\beta^2)(-M_\infty^2 \pm \sqrt{1 - \xi^2}) \tag{2.8}$$

$$\begin{gathered} \xi_{mn} = \tfrac{k}{\beta k_a} \\ \beta = \sqrt{1 - M^2} \end{gathered} \tag{2.9}$$

As the cutoff ratio approaches 1 for the propagating mode, the propagation angle approaches 90^o, and the mode decays. To propagate, a mode cutoff ratio must be greater than 1. Some modal shapes are illustrated for annular and circular ducts, Figure 2.1 and Figure 2.2. The mode characterize the pressure pattern propagating in the duct.

2.3.2 Buffer Zone Approach

The buffer zone technique with explicit damping is rather simpler to apply, although it requires an additional zone of mesh, (Figure 2.3). By explicit damping the solution is driven from reflected plus the incident field to only the incident field towards the outer boundary of the buffer zone. That is, after an iteration is performed, the acoustic field is updated according to;

$$\widehat{Q} = \widehat{\widehat{Q}} - \sigma(x)(\widehat{\widehat{Q}} - \widehat{Q}_{inc}) \tag{2.10}$$

where $\widehat{Q}$ is the updated solution in the buffer zone, $\widehat{\widehat{Q}}$ is the solution after the iteration, $\widehat{Q}_{inc}$ is the desired incident field, and $\sigma(x)$ is a transition coefficient that varies from the interface between the buffer zone and duct to the outer boundary of the buffer zone. In this study another type of damping strategy is also used;

$$\frac{dQ}{d\tau} + R(Q) + \sigma(x)(Q - Q_{inc}) = 0 \tag{2.11}$$

$$\sigma(x) = \sigma(x)_{max}\left(1 + \frac{\triangle x}{L_{ref}}\right)^{\beta} \tag{2.12}$$

where is the Q is the solution matrix , R is the residual matrix, Q_{inc} is the desired incident field and $\sigma(x)$, Equation 2.12,is a transition coefficient that varies from the interface between the buffer zone and the duct to the outer boundary of the buffer zone, L_{ref} is buffer zone length, $\triangle x$ is the difference between grid point x location measured form fan-face and L_{ref}. In the present work, this parameter is varied quadratically from 1 at the interface between the buffer zone and solution domain to 0 at the outer end of the buffer zone. $\sigma(x)_{max}$ is taken as 1 and β is generally taken as 2. Equation 2.12 is an improved form of Equation 2.10.

Acoustic pressure downstream of a circular duct can be expressed in the spinning mode m and circular frequency of ;

$$\widehat{p}(x, r, \theta, t) = \Re \sum_{m,\mu} A^{+}_{m,\mu}[J_m(k_{m,\mu}r) + Q_{m,\mu}Y_m(k_{m,\mu}r)]e^{i\omega t - ik_{x,m\mu}x + i(m\theta)} \tag{2.13}$$

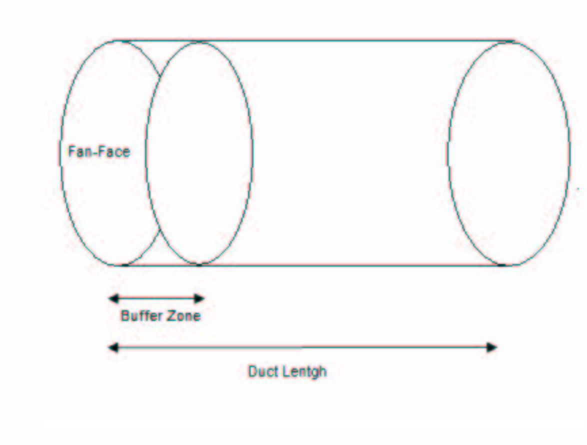

Figure 2.3: Buffer zone in circular duct.

Wave number can be related as in Equation 2.8 and Equation 2.9. The acoustic pressure, Equation 2.13, can be transformed by Fourier Transformation for frequency domain. The transformation leads;

$$\overline{p} = \sum_{m,\mu} A^{+}_{m,\mu}[J_m(k_{m,\mu}r) + Q_{m,\mu}Y_m(k_{m,\mu}r)]e^{-ik_{x,m\mu}x+i(m\theta)} \tag{2.14}$$

Equation 2.14 should satisfy linearized momentum equation, transformed by Fourier-Laplace Transformation. So, application gives the gives these equations in the following form;

$$\begin{aligned} &\tfrac{\partial u}{\partial t} + u_0\tfrac{\partial u}{\partial x} + \tfrac{1}{\rho_0}\tfrac{\partial p}{\partial x} = 0 \\ &\tfrac{\partial v}{\partial t} + u_0\tfrac{\partial v}{\partial x} + \tfrac{1}{\rho_0}\tfrac{\partial p}{\partial r} = 0 \\ &\tfrac{\partial w}{\partial t} + u_0\tfrac{\partial w}{\partial x} + \tfrac{1}{\rho_0 r}\tfrac{\partial p}{\partial \theta} = 0 \end{aligned} \tag{2.15}$$

$$\begin{aligned} &i\omega\overline{u} + u_0 ik^{+}_{x,m\mu}\overline{u} + \tfrac{1}{\rho_0}ik^{+}_{x,m\mu}\overline{p} = 0 \\ &i\omega\overline{v} + u_0 ik^{+}_{x,m\mu}\overline{v} + \tfrac{1}{\rho_0}\overline{\tfrac{\partial p}{\partial r}} = 0 \\ &i\omega\overline{w} + u_0 ik^{+}_{x,m\mu}\overline{v} + \tfrac{1}{\rho_0 r}\overline{\tfrac{\partial p}{\partial \theta}} = 0 \end{aligned} \tag{2.16}$$

The solution of Equation 2.16 for $\overline{u}$, $\overline{v}$, $\overline{w}$;

$$\begin{aligned} &\overline{u} = \tfrac{k^{+}_{x,m\mu}\overline{p}}{\rho_0}(\omega - u_0 k^{+}_{x,m\mu}) \\ &\overline{v} = -\tfrac{\frac{\partial\overline{p}}{\partial r}}{i\rho_0(\omega - u_0 k^{+}_{x,m\mu})} \\ &\overline{w} = -\tfrac{\frac{\partial\overline{p}}{\partial r}}{i\rho_0 r(\omega - u_0 k^{+}_{x,m\mu})} \end{aligned} \tag{2.17}$$

For exhaust duct, the incident field can be equalized to the variables obtained by the method described in the preceding paragraphs, Equation 2.18.

$$\begin{aligned}
&\widehat{\rho_{inc}} = \overline{\rho} = \tfrac{\widehat{p_{inc}}}{c_0^2} \\
&\widehat{p_{inc}} = \overline{p} \\
&\widehat{u} = \overline{u} \\
&\widehat{v} = \overline{v} \\
&\widehat{w} = \overline{w}
\end{aligned} \tag{2.18}$$

2.3.3 Hard Wall Conditions

Fluid particles are allowed to slip at a hard wall under the influence of pressure fluctuations. Numerically, the normal component of the contravariant velocity perturbation is set to zero. That is, on an orthogonal mesh at the wall,

$$\begin{aligned}
&\widehat{V_c} = \eta_x \widehat{u} + \eta_r \widehat{v} \\
&\widehat{U_c} = \xi_x \widehat{u} + \xi_r \widehat{v}
\end{aligned} \tag{2.19}$$

The tangential contravariant velocity perturbation is extrapolated from the interior solution. The azimuthal velocity is extrapolated from the interior solution too. The pressure perturbation can be extracted from the normal momentum balance, assuming the grid lines are orthogonal at the wall surface, as

$$\frac{\partial p}{\partial \eta} = -[2\rho_0 v_{0,t} \widehat{v_t} + \widehat{p}/c_0^2 v_{0,t}][\eta_x^2 + \eta_r^2]^{1/2} R^{-1} \tag{2.20}$$

Where $v_{0,t}$ and $\widehat{v_t}$ are the mean tangential velocity and tangential velocity perturbation, respectively, c_0 is the local speed of sound and R is the radius of the wall curvature, found by using the transformation metrics at the wall.

On the computational domain, the grid is such that the walls and centerline around the engine are settled midway between two grid points. One of them is a ghost point in the wall and the other is first interior point off the wall. This requires interpolation of data to the wall. The third order interpolation is used for a globally fourth order accurate scheme.

2.3.4 Impedance Conditions

On acoustically treated surfaces, liners, a special boundary condition is applied. Because fluid particles are allowed to slip at a wall with a non-zero normal velocity on an acoustic treatment panel, the same momentum equations as the interior domain are solved. The main difference is energy equation which reflects the main role of a liner. The energy equation is obtained from the impedance condition equation, is given as [38]

$$i\omega\widehat{p} + L_0\widehat{p} = -i\omega Z(\omega)\widehat{v_n} \tag{2.21}$$

$$L_0 = U_{0,c}\partial/\partial\xi + \nabla\eta \cdot \partial V_0/\partial\eta \tag{2.22}$$

Where $\widehat{v_0}$ is the normal component of the velocity perturbation, and Z(ω) is the frequency dependent impedance. The spatial operator L_0 of equation above is given in the curvilinear co-ordinates in Equation 2.22. ξ is the grid line along the surface, $U_{0,c}$ is the mean tangential contravariant velocity and V_0 is the mean velocity. when the curvature of surfaces are small, the term L_0 operator can be neglected since its values is usually small.

The equation governing the normal velocity perturbation can be written at the wall as,

$$i\omega\widehat{v_n} + U_{0,c}\frac{\partial\widehat{v_n}}{\partial\xi} + |\nabla\eta|[\frac{v_0}{\eta}\widehat{v_n} + \frac{1}{\rho_0}\frac{\partial\widehat{p}}{\partial\eta} - \frac{\widehat{p}}{\rho_0^2 c_0^2}\frac{\partial p_0}{\partial\eta}] + \frac{2v_{0,t}\widehat{v_t}}{R} = 0 \tag{2.23}$$

where $v_{0,n}$,$v_{0,t}$ and $\widehat{v_t}$ are the mean normal, tangential velocities, the tangential velocity perturbation, respectively. An equation deriving the pressure perturbation along a lined surface can be obtained in the following form with substitution of Equation 2.23;

$$A\frac{\partial^2\widehat{p}}{\partial\xi^2} + B\frac{\partial\widehat{p}}{\partial\xi} + C\frac{\partial\widehat{p}}{\partial\eta} + D\widehat{p} + E = 0 \tag{2.24}$$

where,

$$
\begin{aligned}
A &= \tfrac{U_{0,c}^2}{i\omega Z} \\
B &= \tfrac{U_{0,c}^2}{i\omega Z}[2i\omega + \tfrac{\partial U_{0,c}}{\partial \xi} + |\nabla\eta|\tfrac{\partial v_{0,n}}{\partial \eta}] \\
C &= -|\nabla\eta|/\rho_0 \\
D &= \tfrac{i\omega}{Z} + \tfrac{|\nabla\eta|}{Z}\cdot\tfrac{\partial v_{0,n}}{\partial \eta} + \tfrac{|\nabla\eta|}{\rho_0^2 c_0^2}\tfrac{\partial p_0}{\partial \eta} \\
E &= -2v_{0,t}\widehat{v_t}/R
\end{aligned}
\tag{2.25}
$$

Equation 2.24 is solved on a soft wall after interior and hard wall solutions are updated explicitly at every stage of Runge-Kutta (R-K) algorithm. Equation 2.24 is discretized implicitly in pressure, which results in a linear system of equations. The tangential velocity perturbations required by these equations (*through the E term*) are extrapolated from the available interior solution. In this implicit approach, the pressure amplitudes needed from the interior grid point are set equal to the available values of those obtained explicitly from the R-K stage.

2.3.5 Far-Field Conditions

Non-reflecting boundary conditions are embedded on the outer far-field boundaries. The outgoing waves are damped. The first order spherical damper condition of Bayliss and Turkel [33], *the radiation $B1$ operator*, is used on the inflow parts of these boundaries. On the outflow parts, the linearized momentum equations are solved for the velocity perturbations, but the radiation operator is applied to the pressure perturbation as suggested by Tam and Webb [30]. All farfield boundary conditions are also transformed to the frequency domain in cylindrical coordinates. The operator is arranged as in Equation 2.26. Outflow boundary velocity perturbations are solved by the linearized momentum equations, but B1 operator is applied to pressure fluctuation.

$$
\begin{aligned}
B_1 &= \tfrac{1}{c_\infty \beta}(1 - \tfrac{x}{d}\tfrac{M_\infty}{\beta})\tfrac{\partial}{\partial t} + \tfrac{x}{t}\tfrac{\partial}{\partial x} + \tfrac{r}{d}\tfrac{\partial}{\partial r} + \tfrac{1}{d} \\
\beta &= \sqrt{1 - M^2} \\
d &= \sqrt{(x^2/\beta^2) + r^2}
\end{aligned}
\tag{2.26}
$$

2.3.6 Discretization

Iterative discretization is used effectively in this study. Because, direct solution domain of such a system, including frequency domain governing and boundary conditions, would result in a large linear system of equations with the complex unknowns and to expect an efficient computing for this large system would be not possible. The pseudo time derivative term is added in order to calculate the explicit type algorithms in parallel computing for solution of the present frequency-domain equations. Usage of explicit time integration methods provides convergence acceleration for rapid solutions of the governing equations of the radiation system.

The interior and the farfield boundary equations are written in the form

$$\frac{d\widehat{Q}}{d\tau} + R(\widehat{Q}) = 0 \tag{2.27}$$

Where $R(\widehat{Q})$ represents the semi-discretized governing equations and the farfield boundary conditions in curvilinear co-ordinates, and $d\widehat{Q}/d\tau$ is the pseudo-time derivative term added to calculate the equations explicitly. A four-stage R-K time integration scheme is employed to drive the solution to a steady harmonic state iteratively.

Spatial derivatives are calculated by using fourth order accurate differences. In the cases studied, to obtain results showing the wave propagation, reinforcement or cancellation, or even decay, the mesh characteristic is important. The mesh size should be selected such that it can capture the physical propagation characteristics of the radiation mode, especially for small amplitude. The mesh for the study needed to be rearranged to resolve accurate computation. The R-K scheme is given by,

$$\begin{aligned}
D(\widehat{Q}^0) &= D(\widehat{Q}^n) \\
D(\widehat{Q}^1) &= D(\widehat{Q}^n) - 1/4 \triangle \tau [R(\widehat{Q}^0) - D(\widehat{Q}^0)] \\
D(\widehat{Q}^2) &= D(\widehat{Q}^n) - 1/3 \triangle \tau [R(\widehat{Q}^1) - D(\widehat{Q}^0)] \\
D(\widehat{Q}^3) &= D(\widehat{Q}^n) - 1/2 \triangle \tau [R(\widehat{Q}^2) - D(\widehat{Q}^0)] \\
D(\widehat{Q}^4) &= D(\widehat{Q}^n) - \triangle \tau [R(\widehat{Q}^3) - D(\widehat{Q}^0)]
\end{aligned} \tag{2.28}$$

Where superscript n shows the iteration step, $\triangle\tau$ is the pseudo-time step size from an iteration step to next, and $D(\widehat{Q}^0)$ is artificial dissipation used to suppress the development of spurious waves. A fourth order constant coefficient dissipation model was employed in computations.

2.3.7 Farfield Predictions

A modified version of the Kirchhoff method is employed for farfield sound calculation. The method, given by Farassat and Myers [7], is integrated using a forward time binning approach around a surface, in Figure 2.4. Kirchhoff method is applied for converged solutions by the construction of a 3-D Kirchhoff surface. This surface is constructed by revolving a set of grid lines 360^o around the engine axis. The computed acoustic data on this grid set are distributed over the constructed Kirchhoff surface for one wave period according to Equation 2.29. Then the data on the Kirchhoff surface was integrated for specified farfield observer locations using the Kirchhoff Method.

$$4\pi p_a(x,t) = \int\int_S \left[\frac{E_1}{R(1-M_R)} + \frac{p_a E_1}{R^2(1-M_R)}\right]_{\tau^*} \tag{2.29}$$

where $R = |\overrightarrow{R}|$,$\overrightarrow{R} = \overrightarrow{x} - y(\tau)$,$M_R = \overrightarrow{M} \cdot \frac{\overrightarrow{R}}{R}$, and

The equation below is integrated using a forward-time-binning approach. For a Kirchhoff's surface moving rectilinearly with a Mach vector $\overrightarrow{M}$, this formula is written as,

$$\begin{aligned} E_1 &= -\overrightarrow{n}\cdot \triangledown p_a + (\overrightarrow{M}\cdot\overrightarrow{n})(\overrightarrow{M}\cdot \triangledown p_a) + \left[\frac{\cos\varphi - \overrightarrow{M}\cdot\overrightarrow{n}}{c_\infty(1-M_R) - \frac{\overrightarrow{M}\cdot\overrightarrow{n}}{c_\infty}}\right]\frac{\partial P_a}{\partial\tau} \\ E_2 &= \left(\frac{1-M}{(1-M_R)^2}\right)(\cos\varphi - \overrightarrow{M}\cdot\overrightarrow{n}) \end{aligned} \tag{2.30}$$

The Kirchhoff surface emission times τ^* are found by solving the following equation;

$$\tau - t + \frac{R(\tau)}{c_\infty} = 0 \tag{2.31}$$

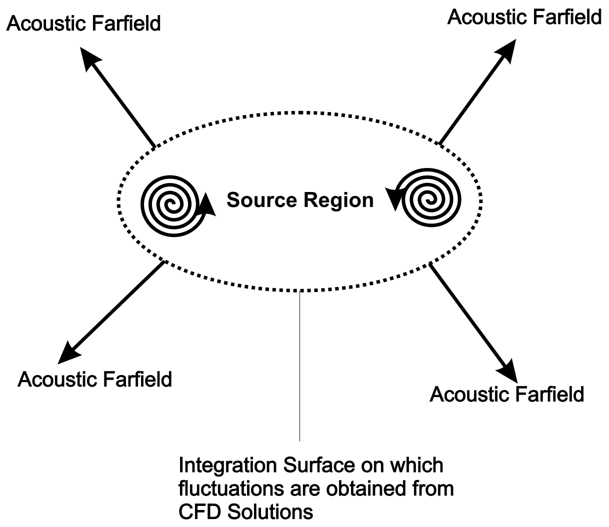

Figure 2.4: Kirchhoff Method

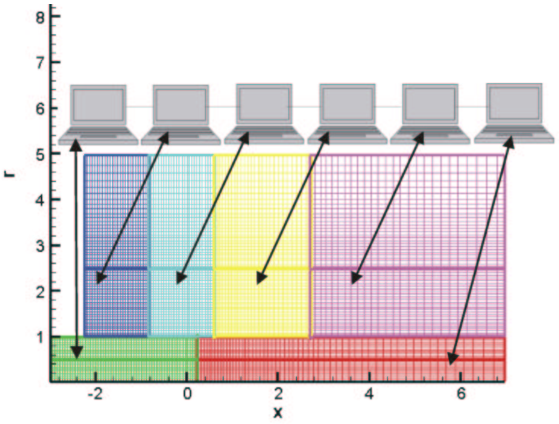

Figure 2.5: Parallel Computation.

2.3.8 Parallel Processing

Parallel processing can simply be described as a method of using more than one computer for the solution of a single problem. Parallelism is generally preferred if the problem consists of large systems of equations to be solved in large domains as in *CFD* applications. CFD tools, especially, require computers with fast processors to perform a large number of calculations within reasonable time and also quite high memory to process great amount of data. However, there is a limit for a computer to meet the above needs, which is generally unsatisfactory. It is possible to overcome this computer limitation by making use of parallel processing so that the computation time to solve a problem is significantly reduced by having several operations, each being a part of the original computation, performed at the same time.

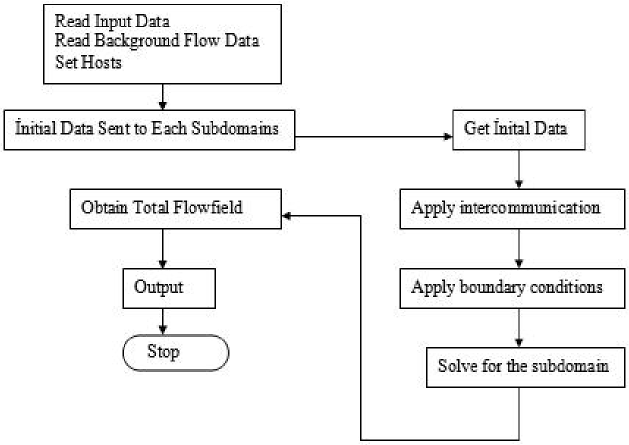

Figure 2.6: Flow Chart for the parallel computation.

Table 2.1: Parallel Computers used for the Project

Computer Name	CPU	RAM	$ProcessorType$	$TotalNumber$
Atmaca	$733MHz$	$512Mb$	$P-3$	8
Albatros	$2.4GHz$	$1.0Gb$	$Xeon$	6

With the recent decrease in the cost of a computer and its accessories, it has become feasible to deploy a cluster of computers as a parallel computing environment. Therefore, parallelism has become a useful approach for attaining very high computation speeds in the last two decades. The computational speed for a specified domain is a function of computations per grid point, operations per second that computer can sustain, number of grid points and processors, etc.

There are mainly two types of parallel computing environments, which are the shared-memory and distributed memory systems. In the shared-memory system, more than one processor share the memory and may perform computational tasks on the parts of the data structure stored in the common memory by either the compiler directives or with the help of new constructs in the programming language. The individual tasks are then executed simultaneously. Task decomposition is possible if there is no data dependency between the tasks to be decomposed from the original computation. The shared-memory approach is generally employed with multi-processor architectures.

The distributed-memory parallel system has a different topology than shared-memory system. In the distributed-memory system, each processor has its own private memory and may perform computations on its own data which subset of the main task, and communicates with other processor for sharing common data. A network computer cluster is the most common environment to construct a distributed-memory system. In this thesis, a distributed-memory parallel algorithm is implemented. In this approach, the computational grid is divided into smaller domains and each sub-domain is assigned to a different dual processor computer running on Linux operating system, which is on a network. The necessary data exchange across a shared boundary between two neighboring sub-domains is realized via library routines form the Message Passing Interface (MPI) standard.The parallel computers used for this study have the technical capacity as shown in Table 2.1. The computation procedure is shown in flow chart 2.6.

CHAPTER 3

RESULTS AND DISCUSSION

3.1 Introduction

In this chapter, the buffer zone technique is discussed with a normal excitation and other numerical approaches for the radiation phenomenon such as direct methods. The buffer zone method is applied effectively in the study. It showed reflected wave absorbtion property with a lower amplitude loss of the radiating mode.

First, the efficiency of buffer zone and characteristic based boundary conditions are discussed for some specific cases. The characteristic based boundary conditions are applied for wave admission on the excitation boundary. But, it is observed for the excitation boundary that do not have buffer zone couldn't handle the reflected waves in the duct. Then the buffer zone technique results are compared with some other numerical results for farfield predictions. The buffer zone length selected sufficiently long boundary for incidence field. The results give an idea about the success of the applied absorbing zone. Effect of flow conditions also discussed and supporting results are stressed.

Both acoustic and mean flow calculations are performed with a cluster of computer enabling parallel computation with MPI library routine. The parallel computation in the subdomains efficiently used with an equal load distributions to each computation processor, by setting nearly same number of grid points in the subdomains.

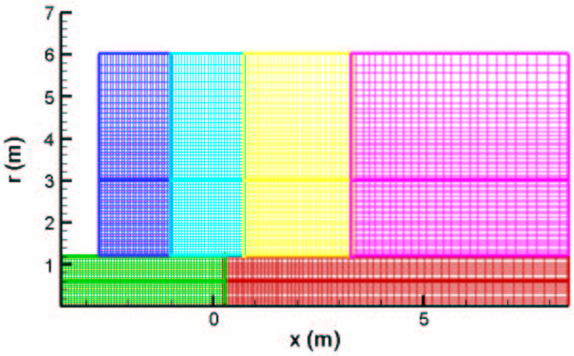

(a) Mesh distribution in subdomains

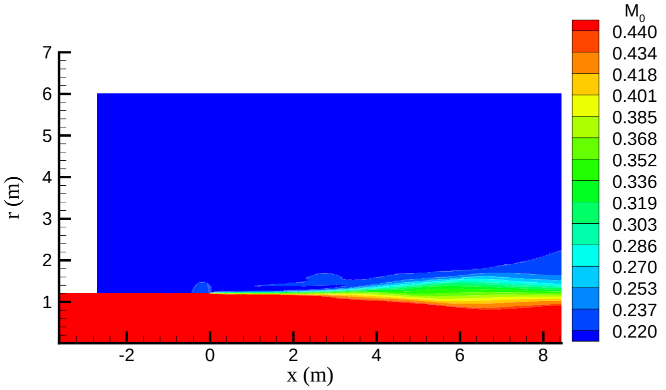

(b) Mean Flow Mach distribution

Figure 3.1: Computational Domain

3.2 Mean Flow Calculations

Acoustic solutions are analyzed for no background and nonuniform background flow in the present study. Background flow is obtained by the solution of 2-D Euler equations for the predetermined domain, Figure 3.1(a). Domain mesh obtained by a commercial program, CFDRC-Geom. Mean flow calculations, Figure 3.1(b) are also practiced in a parallel computational environment. So, the solution reflects the shear layer characteristics for acoustic radiation around aft section.

For the computational domain, diffraction at the duct lip and refraction from shear layer

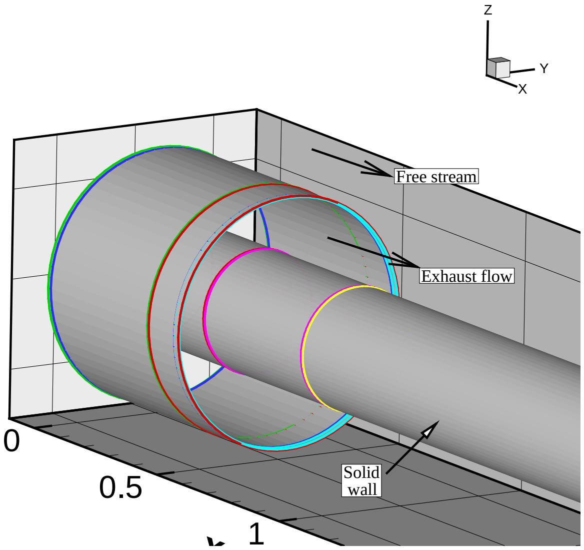

Figure 3.2: Annular Duct Geometry

are the contributions of nonuniform background flow to the acoustic noise radiation at the aft duct section. For no background flow cases, the background flow variables of velocity are set to zero, while mean pressure, temperature and density are set to 101325 Pa, 288 ^oK, 1.225 kg/m^3 respectively. The computational domain is divided deliberately by subdomain boundary line extending from duct lip. This helped for some problems to be set free stream flow values at the whole upper section, and duct values at the whole lower section. This division is chosen because under some geometrical conditions, aerodynamic compression or expansion is small for nearly constant cross sectional ducts. For a nonuniform background flow case with shear layer, mean flow variables are set from Euler solution, an example in Figure 3.1(b). The result includes shear layer, time averaged, which will affect the radiation pattern of sound.

3.3 Acoustic field

3.3.1 Test of Duct Inlet Conditions

The characteristics based and buffer zone based source/boundary conditions are tested using the circular annular duct geometry, Figure 3.2. The hub radius of this geometry is 0.14 m, while the outer wall radius of this geometry is 0.28 m.

One common way of testing boundary conditions is to place the boundary at the different

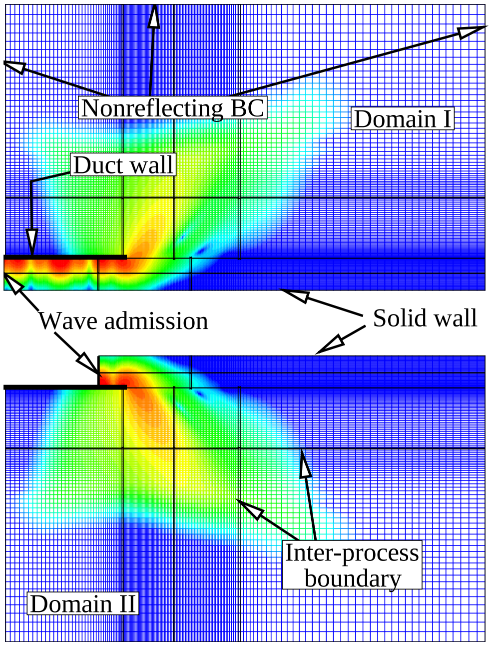

Figure 3.3: Constant cross section, thin walled annular duct. Upper half : long duct , lower half : short duct

locations and observe the effects on the solution. This approach is used for testing the characteristic based duct inflow conditions. Figure 3.3 shows in the upper and lower halves, respectively, a long exhaust duct domain and a short exhaust duct domain, as well as their meshing that was decomposed into subzones for parallel processing. Acoustic waves are introduced at the inlet boundaries in the annular passages. These boundaries are marked as wave admission in Figure 3.3.

The background flow states density, pressure, temperature and the Mach number at the inlet of annular duct are set to 0.75 kg/m^3 , 121950 Pa, 564.5 ^oK, and 0.22, respectively. The entrained flow states from the upstream boundary outside the duct, in the same order, have mean values of 1.225 kg/m, 101325 Pa, 288^oK, and 0.22. the mean flow was computed using the Euler code. The computed mean flow is shown in Figure 3.4. It is clear that due to different flow properties issue into and outside the exhaust duct, shear layer emanates from the duct wall trailing edge. In general, inherent flow instabilities exist in a shear layer, which may be suppressed by the artificial viscosity of the code when they are not very strong. However, when the differences between outside and inside flow quantities are significant, the inherent

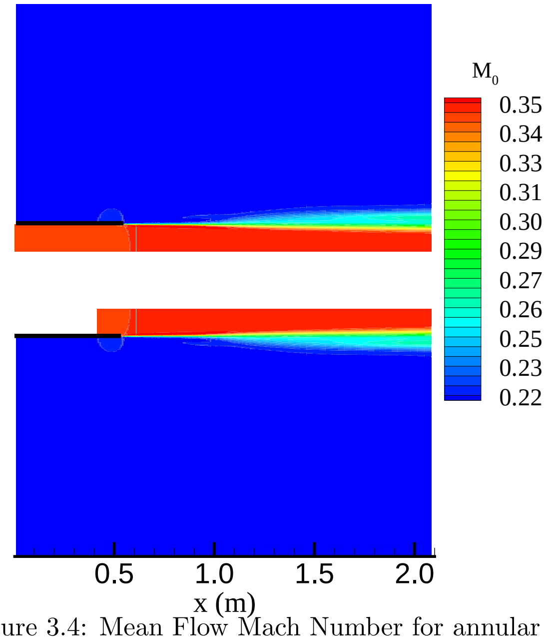

Figure 3.4: Mean Flow Mach Number for annular duct

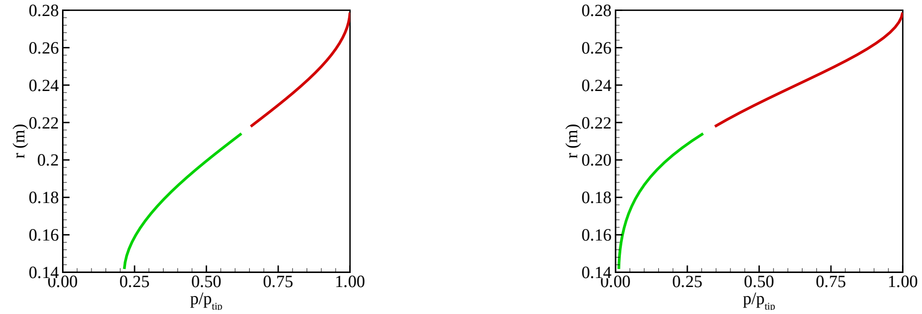

(a) Normalized acoustic source profile for $(6, 0)$ mode

(b) Normalized acoustic source profile for $(13, 0)$ mode

Figure 3.5: Normalized acoustic source profiles

flow instabilities are stronger and it is not possible to control them via artificial dissipation. On the contrary, these instabilities must be allowed for accurate prediction of mean background flow, as they determine the spreading character of the shear layer. Therefore, the mean flow is obtained from the unsteady flow by averaging over time.

Acoustic test of the characteristics based conditions are carried out for two different azimuthal mode orders at different frequencies. These modes are $(6, 0)$ mode at a frequency 3120 Hz and $(13, 0)$ mode at a frequency of 4320 Hz. The corresponding cut-off ratios are 1.583 and 1.096. The modal shapes of the introduced waves are shown in Figure 3.5 for $(6, 0)$ mode and $(13, 0)$ mode. The sound pressure level at the outer wall is set to 130 dB for both modes. The

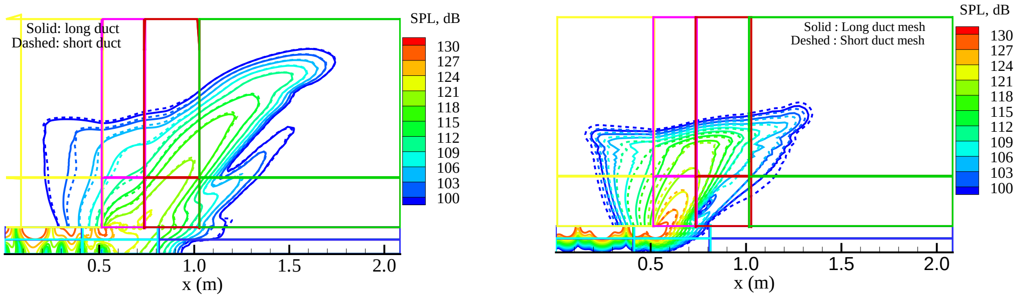

(a) SPL distribution for $(6, 0)$ mode

(b) SPL distribution for $(13, 0)$ mode

Figure 3.6: Normalized acoustic source profiles

computed acoustic fields (SPL contours) of the long and short ducts driven by the mode $(6, 0)$ mode are plotted in Figure 3.6(a). The solid contour lines indicate the acoustic field obtained by the introduction of the waves at the inlet of the long duct, while the dashed contour lines indicate the field resulted by the introduction of the waves from the inlet of the short duct. In the main lobe direction, the agreement between the two acoustic fields is quite good, while there are slight discrepancies in the side lobe directed upstream. The agreement for small side lobe directed at about 45^o from the exhaust also good. However when a similar comparison is made for radiation pattern of $(13, 0)$ mode in Figure 3.6(b), we observe some differences in the main radiation region. Although the main radiation direction has been predicted equally well both for the long and short ducts, the SPLs for the long duct are somewhat lower than for short duct.

The reason for this could be the longer distances that had to be travelled by the waves of the long duct to get to same region as those of the short duct. This may have caused some numerical damping for the waves of the long duct. The other reason could be the inlet conditions by themselves. It is always more difficult to bring waves that are nearly cut-off into solution domain. In fact, we observed rather stronger reflections from the duct for $(13, 0)$ mode. These reflections propagated back upstream and the inlet conditions of the short domain reflected part of them back downstream. This mechanism may be reasonable for the observed differences in the acoustic fields of the short and long ducts for the $(13, 0)$ mode. It should be noted that the employed mesh has a reasonably high resolution. Nevertheless, to understand how much of these differences are actually due to the inlet boundary conditions and numerical damping a

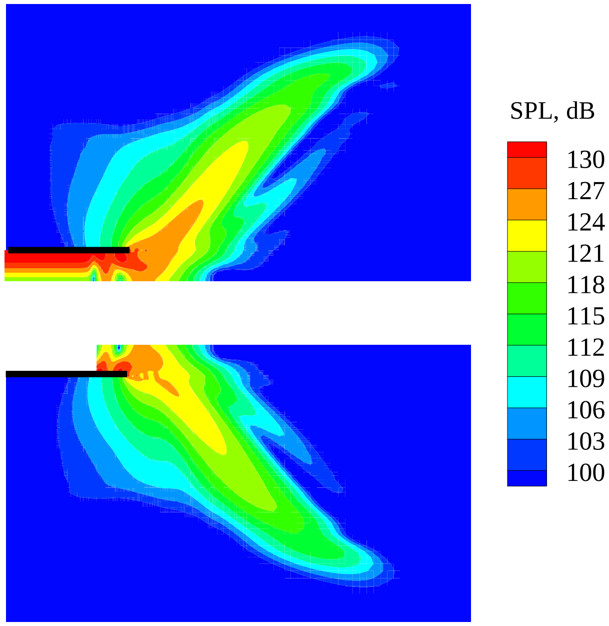

Figure 3.7: Acoustic fields of spinning mode $(6, 0)$ using long duct with buffer zone and short duct with characteristics based boundary conditions at 3120 Hz

grid convergence study must be carried out.

The buffer zone type boundary conditions are also tested using the annular duct. In this technique, the incident acoustic modes are introduced in the buffer zone while upstream propagating waves are absorbed. Figure 3.8 demonstrate an example. In the region marked as buffer zone, the solution obtained by iteration is replaced according equations in Equation 2.10. The transition coefficient factor forces the solution to be composed of only the incident field by the far end of the buffer zone. It is clear that the influence of the upstream propagating waves are quickly diminished in the beginning of the buffer zone (near the interface between the buffer zone and duct domain). Figure 3.7 compares the SPL results obtained for the $(6, 0)$ mode using this technique and characteristics based conditions with the short duct. Upper half of this figure gives the result of the buffer zone application, while the lower part shows the result of characteristics based conditions.

Far-field SPL contour are in particular agreement, while these are slight differences in the near field. These differences become pronounced when a mode is introduced with a cut-off ratio closer to 1. Figure 3.9 compares the computed SPL fields for $(13, 0)$ mode using the buffer

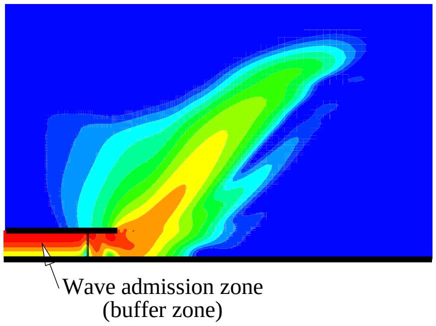

Figure 3.8: Wave admission buffer zone in the duct

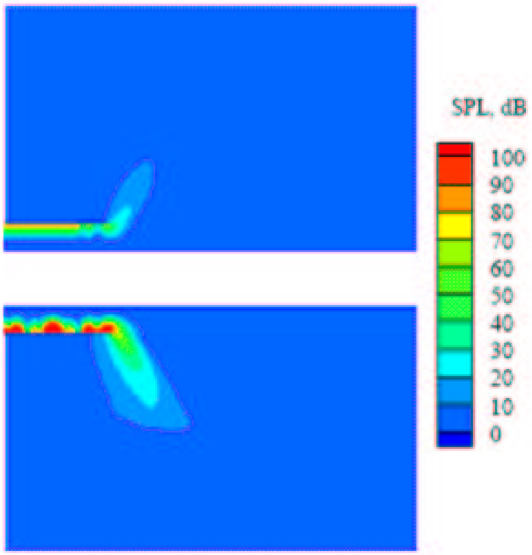

Figure 3.9: Acoustic fields of spinning mode (13, 0) using long duct with buffer zone and short duct with characteristics based boundary conditions at 4320 Hz

zone technique and characteristics based conditions. Upper half again shows the results using the buffer zone, and lower half shows characteristics based conditions. Now the differences between the solutions yielded by the buffer zone and characteristic based conditions are more pronounced. This shows that the characteristics based conditions are not totally reflection free for waves that are nearly cut-off, and therefore must be used carefully.

The high frequency radiation lobe differs from the relatively low frequency radiation pattern. The high frequency noise has a low amplitude characteristic.

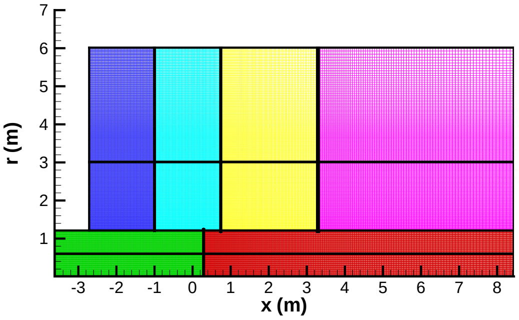

Figure 3.10: Subdomains for Solution Domain

3.3.2 Acoustic Field with no Background Flow

In this section, the buffer zone approach methods will be compared with some numerical data. The solution domain has dimensional characteristic as; hub radius of 1.22 m, with no center body. Direct method results are also compared for this case. All numerical calculations are performed for 12 subdomains for this mesh geometry, Figure 3.10.

For no mean flow case, background pressure, temperature and velocities are set to 101325 Pa, $288^o K$and zero respectively, in and around the duct. At fan stage, speed of sound is taken as 340 m/s. The acoustical radiation performed for $(10, 0)$ mode, for frequency 960 Hz and cut-off ratio 1.82, Figure 3.11. Acoustical results are evaluated by buffer zone method applied as Equation 2.11. The explicit damping approach is improved. And the improved approach worked with success.

Frequency domain results for density, velocity and pressure fluctuations show peak lobe at around 40^o from the duct end. This lobe determines the radiation characteristic of the mode for the present geometry and flow conditions. The maximum amplitude of fluctuations radiate in this direction when leaving the duct end. Acoustic mode propagating in the duct has an wave angle of 29^o. The propagating mode spins in the duct at this angle. The defraction effect of the duct lip causes the propagating waves to radiate at a higher angle after duct end. Another important parameter for the mode is cut-off ratio. Cut-off ratio is fraction which reflect the mode will propagate or not. The ratio also gives an idea about the propagation of the wave around the duct, because it reflects the angle at which the mode spins in the duct. Figure 3.12 illustrates the profile of the mode in the duct.

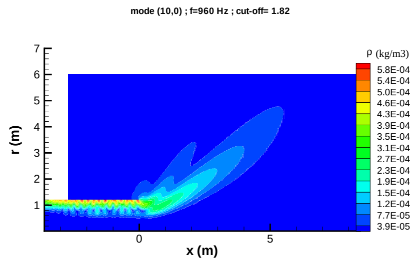

(a) Density fluctuation

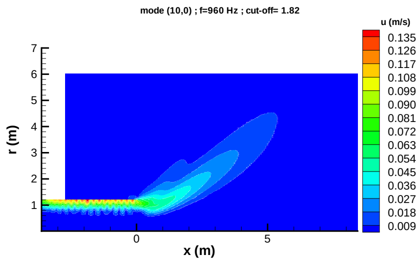

(b) u velocity fluctuation

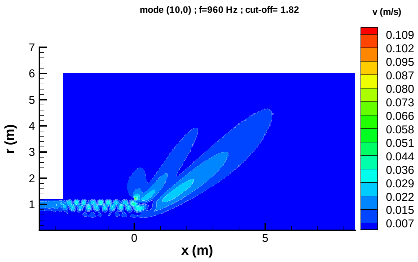

(c) v velocity fluctuation

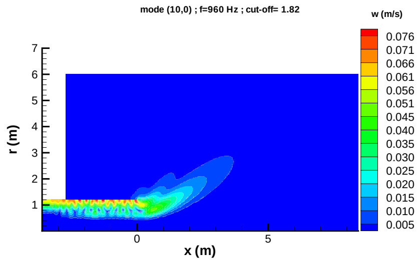

(d) w velocity fluctuation

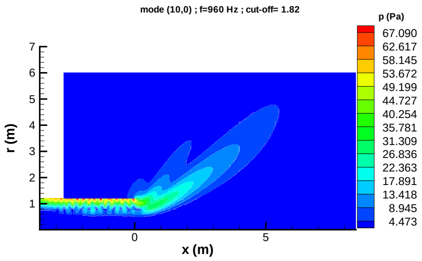

(e) Pressure fluctuation

Figure 3.11: Acoustic field of mode $(10, 0)$, f=960 Hz, cut-off=1.82

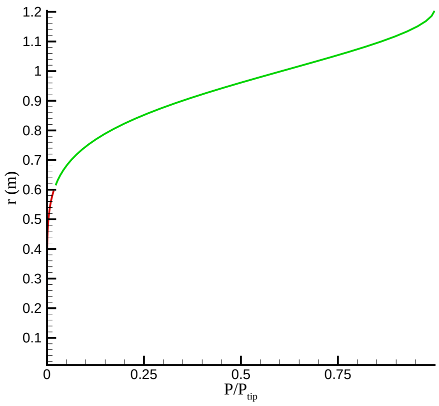

Figure 3.12: Normalized acoustic source profile for $(10, 0)$ mode.

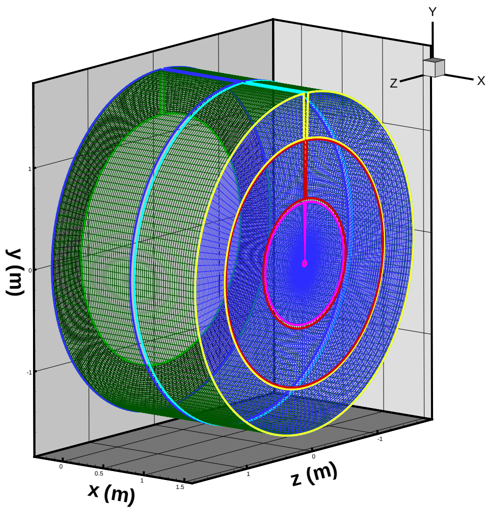

(a) Kirchhoff Mesh

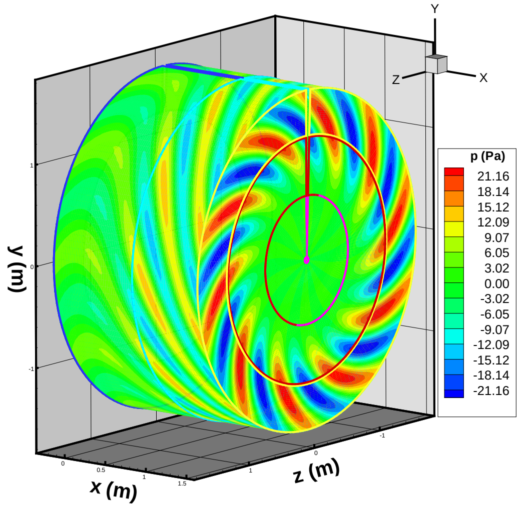

(b) Selected Kirchoff surface acoustic data for farfield calculation

Figure 3.13: Kirchhoff Surface for mode $(10, 0)$

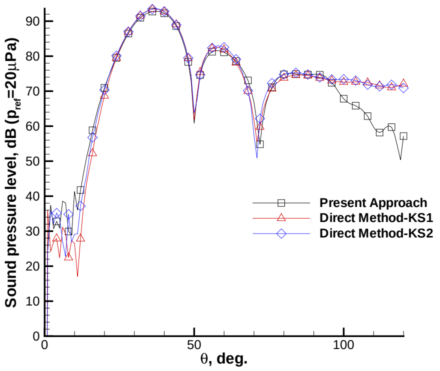

Figure 3.14: Farfield Sound Pressure Levels for direct and frequency domain approaches for $(10, 0)$ mode, f=960 Hz

Farfield calculations are performed for most of the acoustical computation. In this study, Kirchhoff farfield approach is applied for the computational domains. The Kirchhoff surface selected for the computational domain has the acoustic data on itself, Figure 3.13. Farfield directivity draws a similar pattern with previous fluctuations' radiation, Figure 3.11. The comparison is made with a direct method approach calculation performed for the same duct geometry and flow conditions, Figure 3.14. Both methods have similar radiation direction especially at maximum amplitude radiation direction. θ is the angle from duct line. This angle will describe direction of the maximum amplitude from duct end. Direct method calculations require finer mesh distribution and it is expensive for numerical calculations.

Amplitude characteristic of the radiating mode are similar for both direct and frequency domain approach. The oscillation around $100^o - 110^o$ is an expected condition. Because mesh resolution at this direction for the computational domain is not enough. As the direct frequency domain approach has a finer mesh, the resolution makes the computations more efficient for this larger angles. Stretching of mesh in solution domain can cause some source of numerical error. Direct method result are obtained from an ongoing project study. In general, both direct and present frequency domain approaches have same propagation pattern for farfield. Multiplication of calculated acoustic fluctuations by $e^{i\omega t}$, time harmonic, will draw a time history of the propagating mode, Figure 3.16.

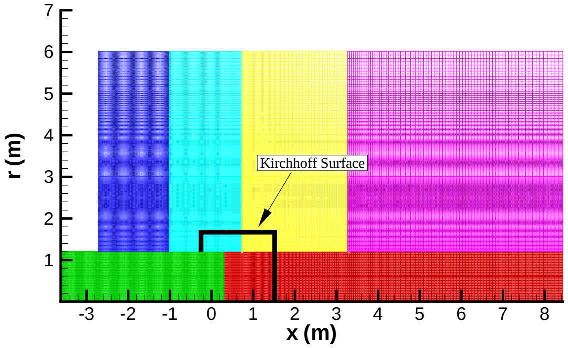

Figure 3.15: Kirchhoff Surface on Solution Mesh

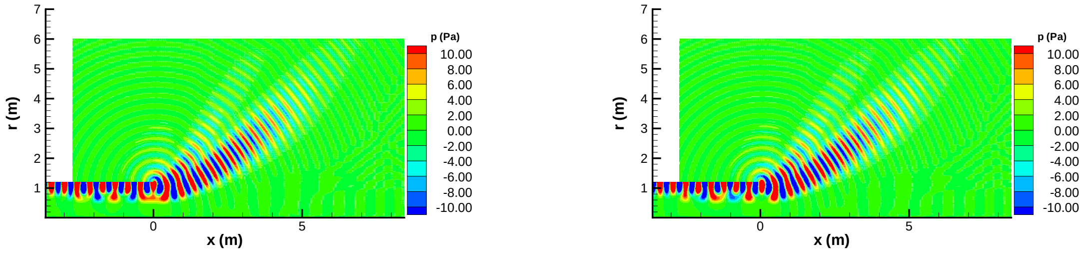

(a) at t=t_o

(b) at t=$t_o + \frac{4}{24}T$

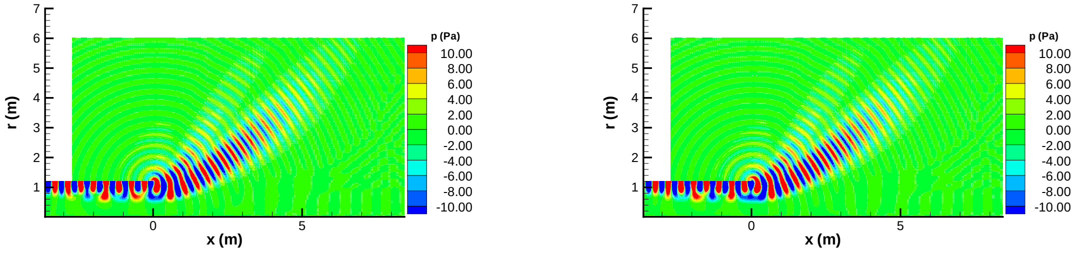

(c) at t=$t_o + \frac{8}{24}T$

(d) at t=$t_o + \frac{12}{24}T$

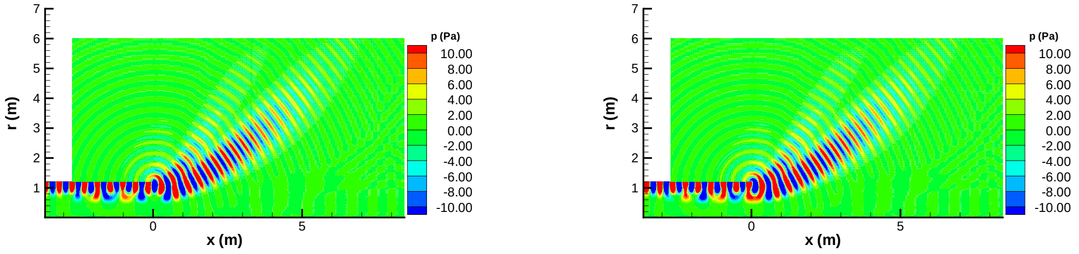

(e) at t=$t_o + \frac{16}{24}T$

(f) at t=$t_o + \frac{20}{24}T$

Figure 3.16: Time Harmonic Propagation for mode $(10, 0)$, f=960 Hz (T= period of the wave)

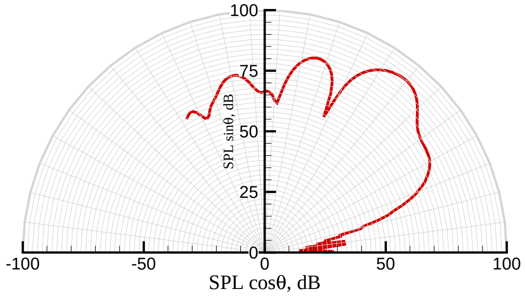

(a) Radiation polarity

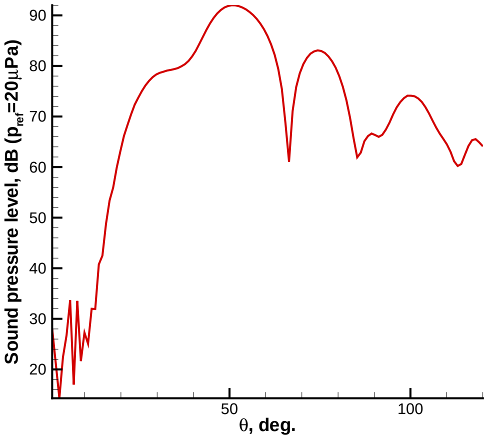

(b) Radiation directivity

Figure 3.17: Farfield directivity for mode $(10, 0)$, f=860 Hz, $R = 50$ m

3.3.3 Acoustic Field with Background Flow

The same propagation mode $(10, 0)$ analyzed for a non zero background case for frequency 860 Hz. The background flow at the lower part of the duct line has temperature, pressure, and Mach number values $300^o K$, 100590 Pa and 0.46 respectively. Upper part of the domain have a temperature, pressure, Mach number values $288^o K$, 101325 Pa and 0.22 respectively. These values are set without computing mean flow.

Farfield calculations are performed with a Kirchhoff surface forming a mesh as shown for no background flow case. Surface is placed in fine mesh part of computational domain, Figure 3.15. This will basically decrease the amplitude loss for farfield calculations. Radiation directivity, Figure 3.17(a), shows a peak radiation lobe at around 55^o while wave angle is 49^o. Although the frequencies are a bit different from the previous case the refraction cause the mode to propagate

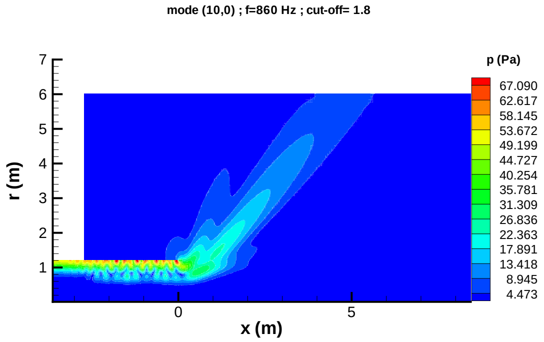

Figure 3.18: Pressure for $(10, 0)$ mode, $f = 860$ Hz

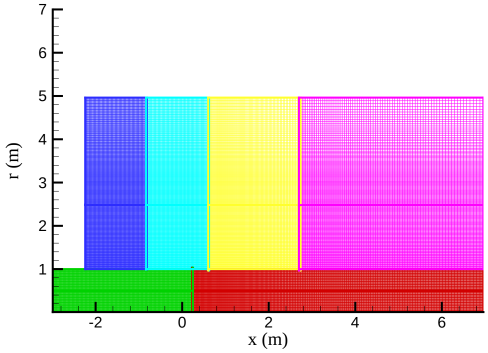

Figure 3.19: Solution Domain

at a higher θ angle. In this case, frequency is increased and background flow conditions are changed from the previous case. As frequency increased wave angle in the duct at which the propagating mode spins increases and cut-off ratio decreases. The increase of wave angle causes the mode after propagation to radiate at a higher angle of attack, 49^o.

3.3.4 Buffer Zone and Characteristic Based Boundary Conditions Application

Buffer zone absorbs the reflected waves in the duct. The characteristics based boundary condition and buffer zone boundary conditions are tested for a no background case, in which background pressure, temperature and velocities are set to 101325 Pa, 288 K, and 0 respectively. Geometry of domain is in Figure 3.19. For this calculations reference wall amplitude is set to 130 dB for duct wall. Mode $(13, 0)$ is analyzed for $f = 1250\ Hz$. This results will reflect the effectiveness of buffer zone over characteristic based boundary conditions. The mode profile gives idea about propagation pressure pattern near the duct wall, Figure 3.20. As the profile is

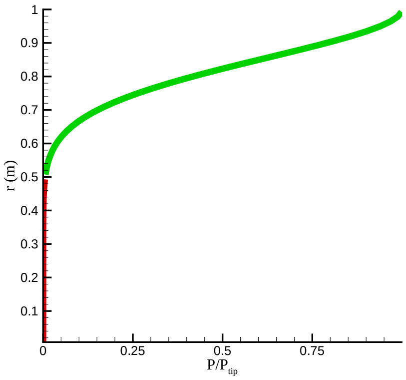

Figure 3.20: Normalized acoustic source profile for $(13, 0)$ mode

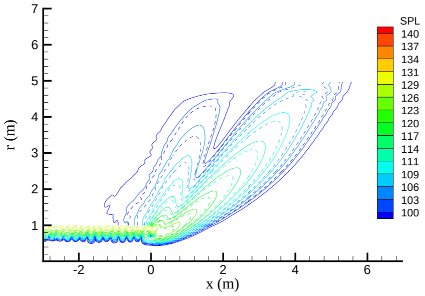

Figure 3.21: SPL for $(13, 0)$ mode, $f = 1250$ Hz, dashed line = buffer zone BCs, line= characteristic BCs

nearly on the duct wall surface, there should be enough number of mesh point covering the both acoustical amplitude and wavelength to transfer the acoustic data numerically. For this reason, point per wavelength is taken as 14 in this case. Farfield SPL of both boundary conditions for $(13, 0)$ mode at a distance of 100 m illustrated in Figure 3.22.

For compared two cases, the pressure pattern also shows in a similar fashion. But, it is seen that there is a magnitude difference, about $3 - 4$ dB, between the two boundary conditions at peak radiation direction. Overall farfield directivity pattern is so similar, Figure 3.21. If we look results for a distance 50 m, the magnitude of difference between the levels can be found at nearly equal to the one for 100 m. As the sound level at a distance from its source is inversely proportional to radius, the amplitude loss will be felt at a higher level for nearer farfield solution.For R= 50 m, farfield directivity is as in Figure 3.23.

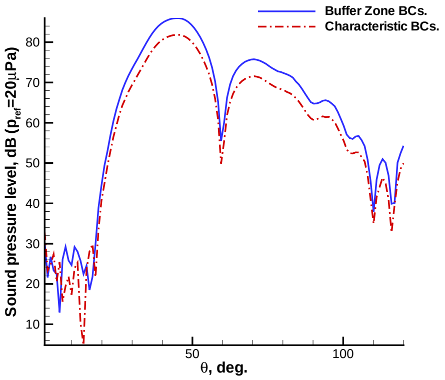

Figure 3.22: Radiation directivity for $(13, 0)$ mode, $f = 1250$ Hz, $R = 100$ m

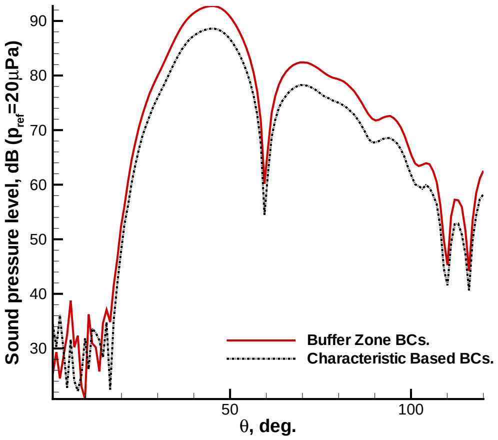

Figure 3.23: Radiation directivity for $(13, 0)$ mode, $f = 1250$ Hz

3.3.5 Acoustic Field for a Mode of lower Cut-Off

For determination of effectiveness of buffer zone, the mode propagation pattern is selected such that it is nearly cut-off. The purpose of the buffer zone is to absorb numerically generated reflected waves in the duct. The reflection effect in the duct can be large. Especially, for the modes that has a cut-off value near to 1 has a wave angle in the duct near to 90^o. This will make the waves reflect easily. Comparison of cases, one with characteristic based boundary conditions and the other with buffer zone, can give idea about the phenomena. The solution domain is an annular duct with outer and inner radius 1.22 m and 0.97 m respectively, $\sigma = 0.77$. The mesh has 39904 cells. The domain is divided into 14 subdomains, Figure 3.24. The background flow at the lower part of the duct line has temperature, pressure, and Mach number values $300^o K$,

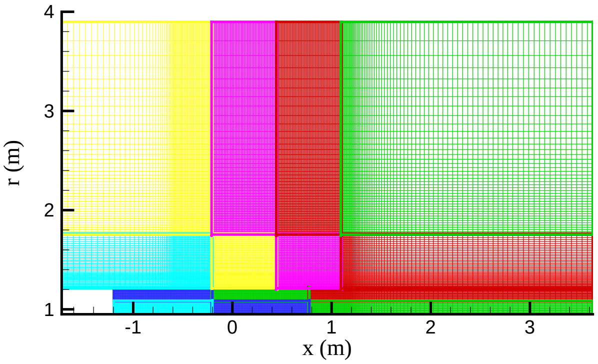

Figure 3.24: Mesh for $(17, 0)$ mode.

100590 Pa and 0.46 respectively. Upper part of the domain have a temperature, pressure, Mach number values $288^o K$, 101325 Pa and 0.22 respectively.

Mode $(17, 0)$ has cut-off value 1.15, wave angle 88^o, frequency 870 Hz. Propagation pattern with buffer zone shows radiation direction at nearly 85^o, Figure 3.25.

Farfield directivity is calculated by a Kirchhoff surface around the duct, Figure 3.26. Kirchhoff surface has a mesh distribution for the case as in Figure 3.27. Obtained Kirchhoff surface acoustic pressure is illustrated in Figure 3.28. The obliquity of pressure pattern on the Kirchhoff surface around the corners is decreased because of the peak radiation around 90^o. Amplitude is on the upper side of the cylinder consisting Kirchhoff surface. The farfield sound propagation pattern shows peak lobe is around 86^o from the duct end, Figure 3.29.

This high radiation angle is the result of the spinning mode in the duct. This mode has a wave angle around 88^o. So the peak radiation lobe is nearly 90^o. The radiation occurs at angles greater than 90^o. The amplitude around these large angles are larger than the one with lower cut-off ratio, Figure 3.30.

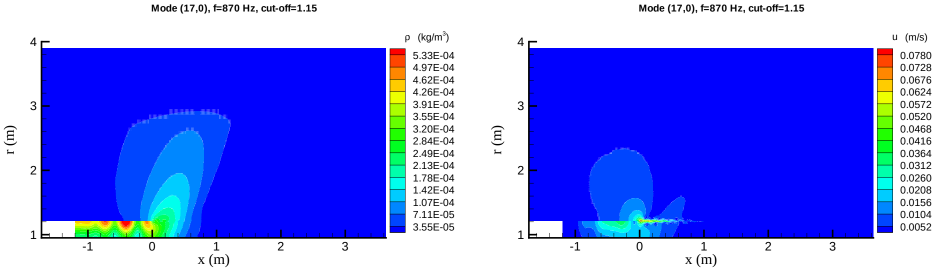

(a) Density fluctuation.

(b) u velocity fluctuation.

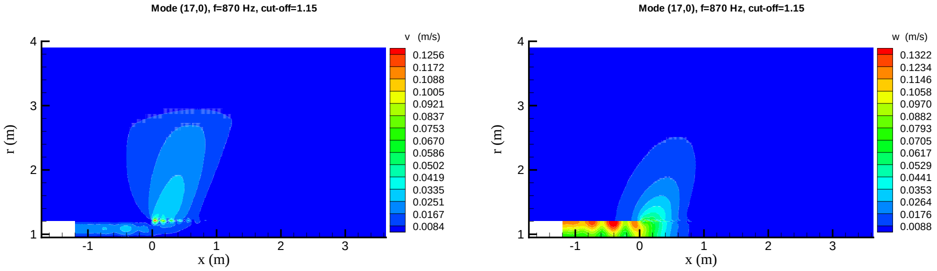

(c) v velocity fluctuation.

(d) w velocity fluctuation.

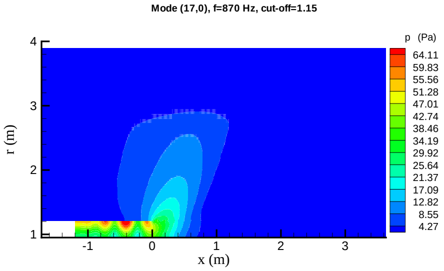

(e) Pressure fluctuation.

Figure 3.25: Acoustic field of mode $(17, 0)$ at 870 Hz

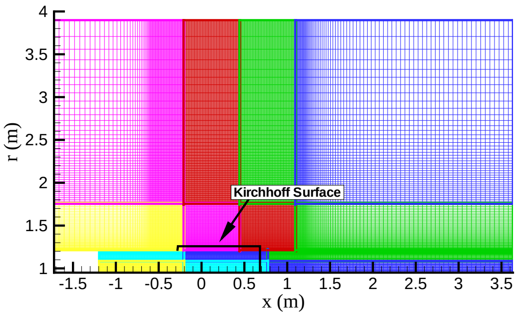

Figure 3.26: Kirchhoff surface on the mesh for mode $(17, 0)$

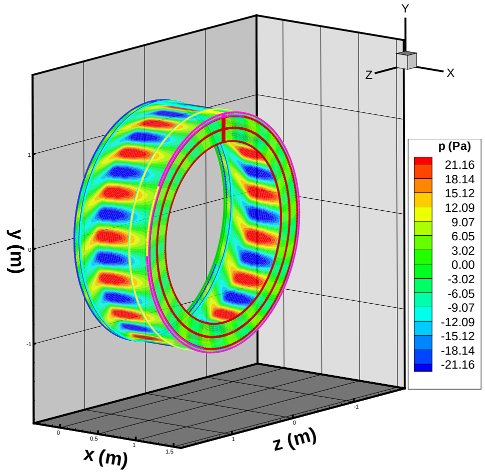

Figure 3.28: Kirchhoff surface pressure field for mode $(17, 0)$

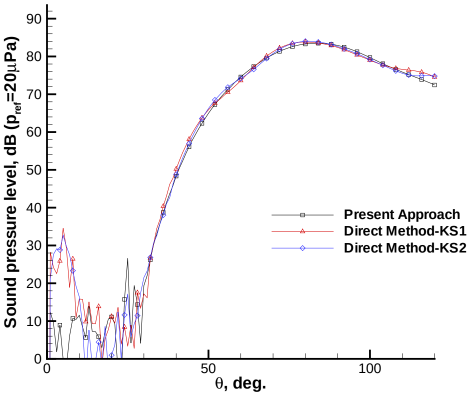

Figure 3.29: Farfield directivity of buffer zone and characteristic boundary conditions for $(17, 0)$ mode

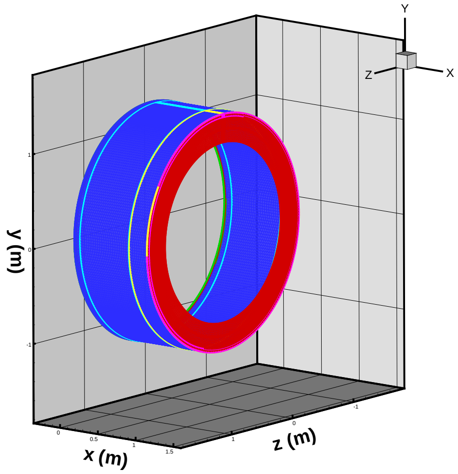

Figure 3.27: Kirchhoff surface mesh for mode $(17, 0)$

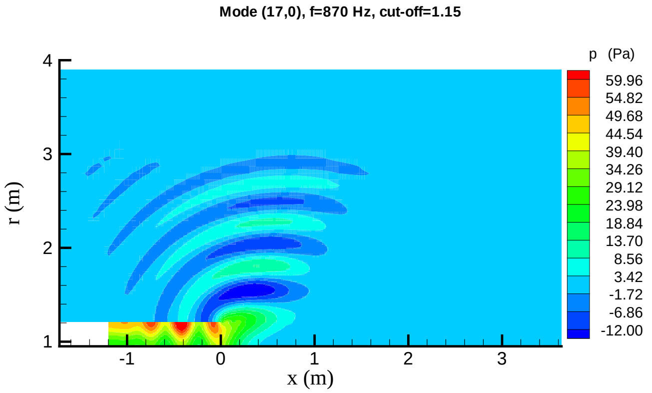

Figure 3.30: Instantaneous pressure field for mode $(17, 0)$

Now the same background flow parameters for the one with buffer zone is set for a characteristic based boundary condition case. Mode (17,0) radiation pattern for characteristic based boundary condition will help to see the effect of the wave reflection in the duct. For the same domain mesh, obtained acoustic pattern is as in Figure 3.31. General pattern seems same as the one with buffer zone, Figure 3.25. But, the farfield calculations shows the effect of Buffer zone on reflected waves. The farfield directivity of characteristic based solution is affected by reflection, Figure 3.32. Although Kirchhoff surface is same, the acoustical data used over the surface differ between two cases. This is mainly by the refections in the duct. The peak radiation direction occurs at nearly the same as with buffer zone. But, there is an amplitude error nearly over all angle range.

This comparison emphasize the fact that buffer zone absorbtion phenomena is dependent on wave angle. As the cut-off ratio decreases the reflection absorbtion by buffer zone become superior over characteristic based approach. The reflection in the duct because of the wave reflection is high for cut-off ratios near to 1. Besides, characteristic based boundary condition should be applied carefully for the cases nearly cut-off.

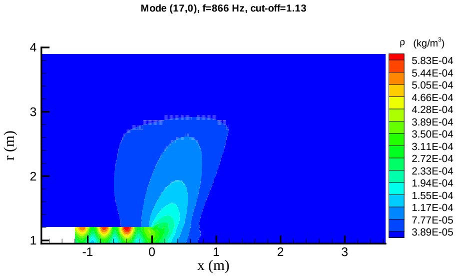

(a) Density fluctuation

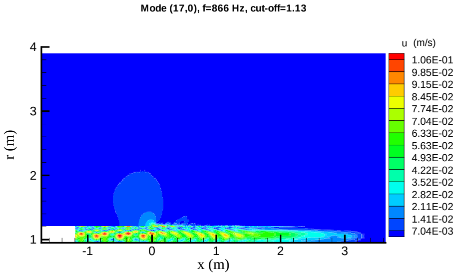

(b) u velocity fluctuation

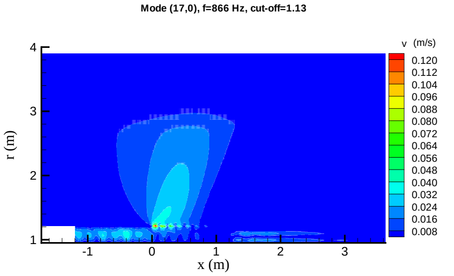

(c) v velocity fluctuation

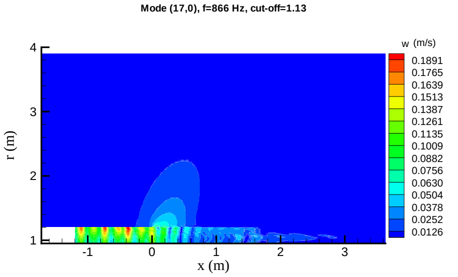

(d) w velocity fluctuation

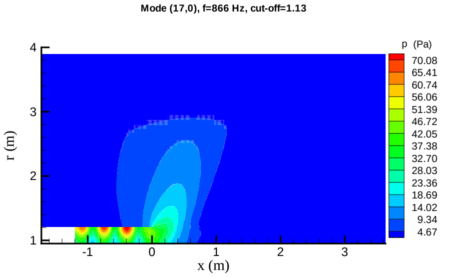

(e) Pressure fluctuation

Figure 3.31: Acoustic field of mode $(17, 0)$ at 870 Hz

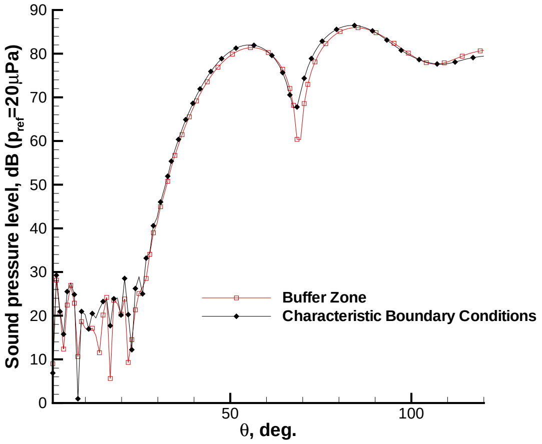

Figure 3.32: Farfield directivity for $(17, 0)$mode, with buffer zone and characteristic boundary conditions

3.3.6 Effect of Buffer Zone Length on Acoustic Field

Buffer zone length should be carefully chosen for the propagating mode. The length of the Buffer zone is to be enough for the wavelength. The buffer zone uses incident field data for the mode. Reflections in the duct can be absorbed by a sufficient length of buffer zone, covering the distance of its wavelength. Mode $(17, 0)$ is tested for three cases. All three case have background flow at the lower part of the duct line has temperature, pressure, and Mach number values 300^oK, 100590 Pa and 0.46 respectively. Upper part of the domain have a temperature, pressure, Mach number values 288^oK, 101325 Pa and 0.22 respectively. Subdomain at the engine exhaust boundary has 117 grid points in x direction. The first case is chosen to start at 90^{th} grid point counted from right boundary of the subdomain and to end at 117 at the engine exhaust boundary. Second case is chosen to start at 41^{th} grid point counted from right boundary of the subdomain and to end at 117^{th} grid point at the engine exhaust boundary. Last case is chosen to start at 5^{th} grid point counted from right boundary of the subdomain and to end at 117^{th} grid point at the engine exhaust boundary. These cases cover the wavelength of the mode from the duct exhaust boundary. Cases are illustrated on the mesh in Figure 3.33. The graph is zoomed at maximum amplitude to see the effect in Figure 3.35.

Farfield characteristics of these three cases is illustrated in Figure 3.34. The figure clarifies the fact that while using buffer zone in our solution domain in the duct, the incidence field

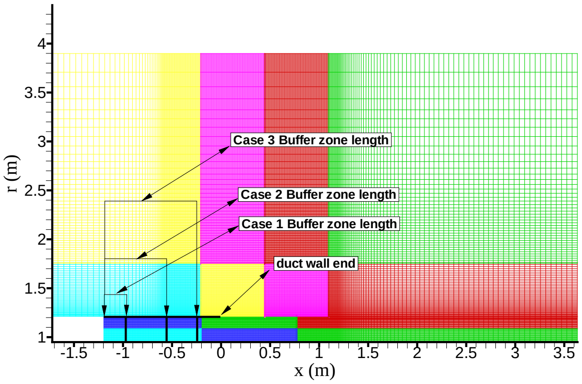

Figure 3.33: Mesh for $(17, 0)$ mode

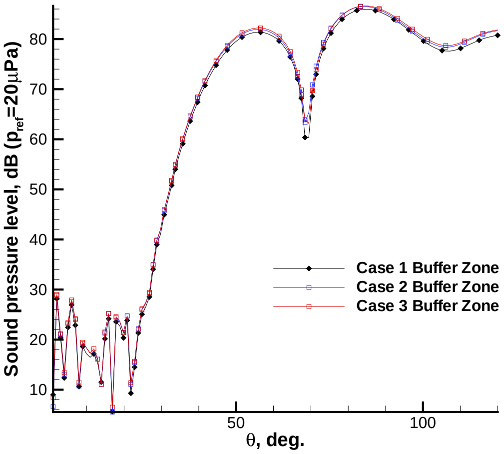

Figure 3.34: Farfield Radiation for 3 selected buffer length

data is used for absorbtion of the reflected waves. Arranging the length of the buffer zone sufficient for the propagating mode, we guarantee that the incident field is used to update the computational domain over the wavelength of the mode in the duct. As the buffer length decrease, it behaves like normal characteristic boundary conditions as discussed before. This is an expected result, such that; as buffer length decreases its capability to absorb the spurious waves decreases. It seems that optimum length is determined by looking at pressure pattern in the duct. The mode wavelength is a determining factor.

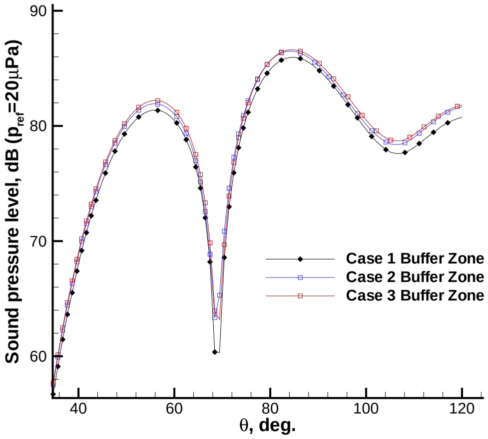

Figure 3.35: Farfield Radiation for 3 selected buffer length, zoomed at maximum amplitude

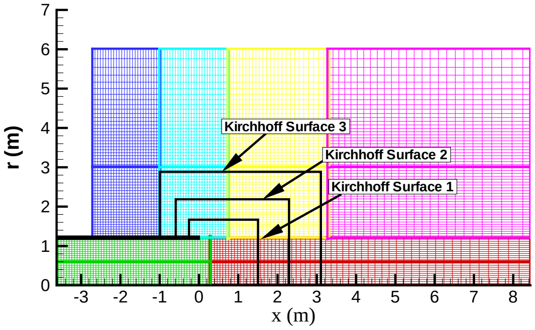

Figure 3.36: 3 Kirchhoff Surfaces,for $(10, 0)$ mode

3.3.7 Farfield Calculation for different Kirchhoff Surfaces

For farfield calculations, Kirchhoff integration surface is used. The surface is selected covering the duct in a fine mesh region possessing the maximum lobe for the propagating mode. The acoustic data on the surface is integrated to find the farfield directivity pattern.

For the case, mode $(10, 0)$, 3 possible Kirchhoff surfaces, Figure 3.36, are analyzed for no background flow case. Results includes buffer zone application for the duct exhaust boundary. No background flow in which background pressure, temperature and velocities are set to 101325 Pa, $288^o K$, and 0 respectively.

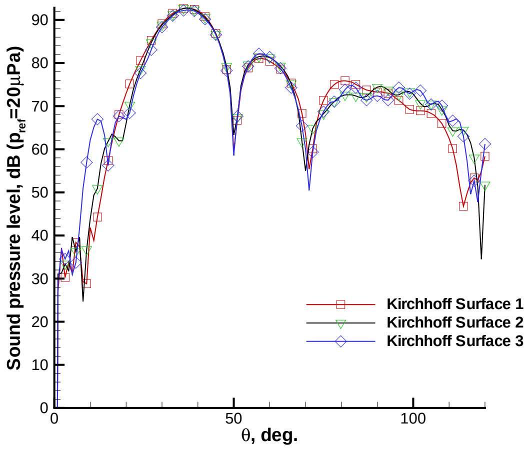

Figure 3.37: Farfield directivity of 3 Kirchhoff Surfaces,for $(10, 0)$ mode, $R = 50$ m

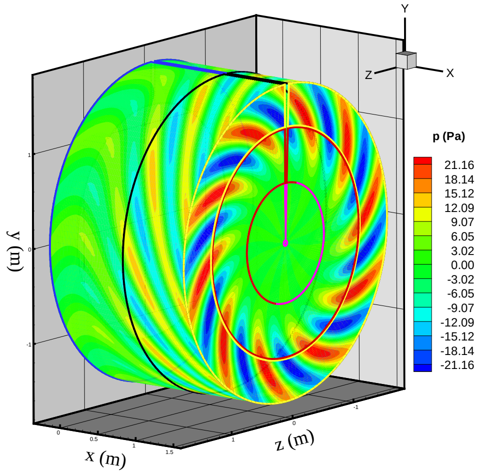

Figure 3.38: Kirchhoff surface 1 pressure distribution,for $(10, 0)$ mode

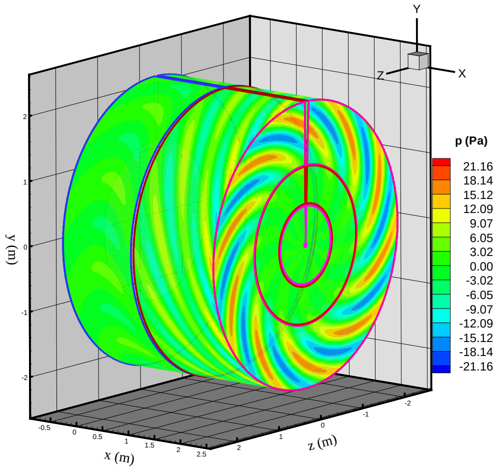

Figure 3.39: Kirchhoff surface 2 pressure distribution,for $(10, 0)$ mode

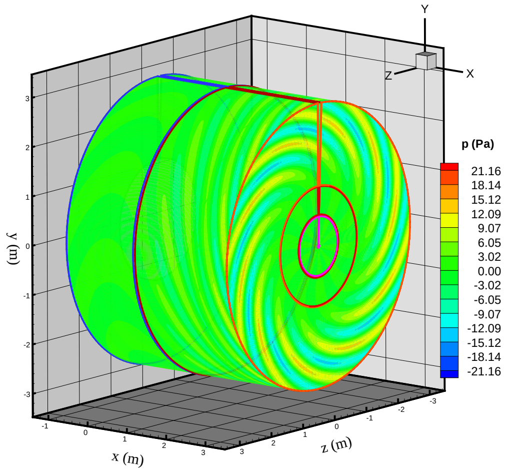

Figure 3.40: Kirchhoff surface 3 pressure distribution,for $(10, 0)$ mode

Kirchhoff surfaces for the mode shows a propagation pattern as in Figure 3.38, Figure 3.39, Figure3.40. Figure 3.37 summarize that selected surfaces capture amplitude and radiation angle properties at the radiation peaks for the mode. Some oscillations are results of mesh pattern. On Kirchhoff surface 3, resolution of mesh changes more rapidly than the other surfaces. Especially, at high angles of calculations oscillation amplitudes are high. At 100^o, comparing Kirchhoff surface 3 and 1, Figure 3.37, it can be said that pressure fluctuations calculated differs by a factor nearly 1.6. Selected Kirchhoff surfaces is not affected from mesh stretching property of the domain especially at maximum radiation angles. Kirchhoff Surface 1 is used in farfield calculations.

3.3.8 Effect of Background Flow on Acoustic Radiation

Farfield directivity for mode $(9, 0)$ is analyzed with background flow case for buffer zone boundary and characteristic boundary conditions. Background flow is obtained from Euler solution. Freestream mach number, density, temperature and pressure at fan stage are 0.22, $1.17 kg/m^3$, $300^o K$, 100590 Pa. Propagating mode has cut-off ratio and frequency 1.76, 766 Hz, respectively. Normalized pressure is as in Figure 3.41. Obtained freestream mach number distribution is in Figure 3.42. Shear layer is obtained with time averaging method, to speed up the convergence of unsteady phenomenon, shear layer.

Obtained farfield directivity pattern of buffer zone and characteristic based boundary con-

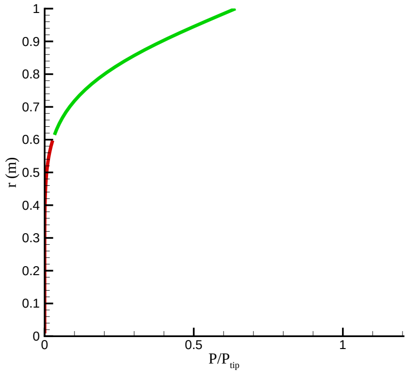

Figure 3.41: Normalized acoustic source profile for $(9, 0)$ mode

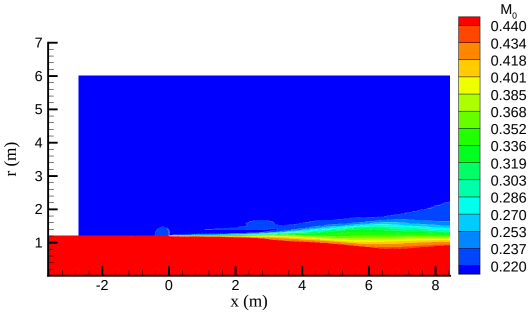

Figure 3.42: Mean flow Mach number distribution

ditions for this case is illustrated in Figure 3.43. This case will illustrate the effect of shear layer. Also, the effectiveness of buffer zone over characteristic based boundary condition for nonuniform background case will be examined. Shear layer will cause acoustic waves to have rarefaction after the duct end. Also farfield directivity at the maximum radiation lobe are nearly same. But, magnitude of fluctuations are about 4 dB in difference. This difference means that pressure fluctuations calculated with buffer zone and with characteristic based boundaries differ by a factor 1.6. Absorbtion of spurious waves in the duct turns out to have higher amplitude fluctuations at farfield. Also, fluctuations at farfield in Figure 3.43 at higher angles are reduced because of absorbtion of reflected waves.

For some of previous cases, uniform background flow case is applied such that the background flow variables are set at the upper and lower part of the duct without Euler solution,

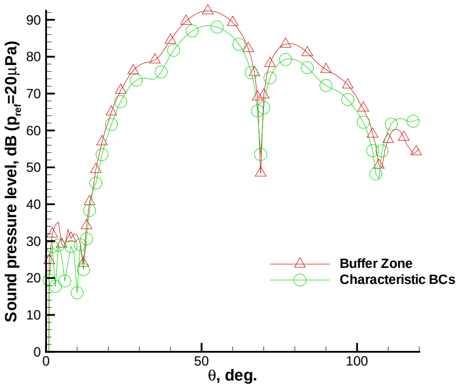

Figure 3.43: Farfield directivity of mode $(9, 0)$ with diffused shear layer, R=50m

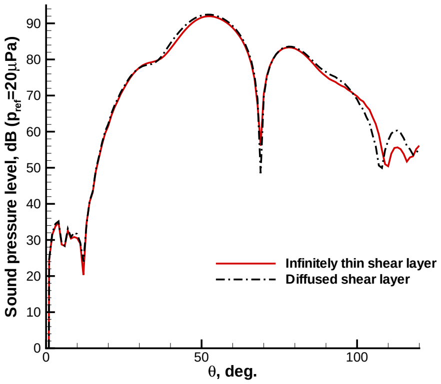

Figure 3.44: Farfield directivity of diffused and infinitely long shear layer with buffer zone, R=50m

infinitely long shear layer. Comparison between infinitely long shear layer and diffused shear layer obtained from Euler solution will reflect the effect of shear layer to farfield noise. Figure 3.43 is farfield directivity of diffused shear layer. Comparison between infinitely long and diffused shear layer farfield results are in Figure 3.44. This comparison shows us the effect of shear layer to farfield radiation. Shear layer effects are rarefaction and continuous reflection properties. These effect are as seen from Figure 3.44. The difference between two cases is not so big as the one with characteristic based case. The maximum lobe direction is nearly same. The thickness of shear layer is not effective so much to radiation pattern of the acoustic mode.

CHAPTER 4

CONCLUDING REMARKS

Acoustic radiation and propagation problem around exhaust duct is calculated in frequency domain with linearized Euler equations. Computations includes both uniform and non uniform background cases. A pseudo time derivative term is added to the frequency domain equations so that a time marching technique can be employed to drive acoustic field to steady state explicitly by Runge-Kutta time integration. Farfield directivity of propagating sound is calculated by Kirchhoff method. All computations are performed in parallel computers using `MPI` library routines in a computer cluster. Different acoustic modes and cut-off ratios are examined. Buffer zone technique is applied and compared with characteristic based boundary conditions. Some numerical results of this explicit frequency domain approach are compared with direct method in frequency domain.

Some background flow cases are also investigated. These include no background flow case, uniform background case and background flow obtained by the solution of 2-D Euler equations. Because the duct geometry is not so effective on compressibility, infinitely long shear layer approach is generally analyzed, saving solution time. Mean flow also affect the sound propagation such that radial wavenumber in r direction is not so affected, but axial wavenumber in x-direction is increased. This will enforce us to have finer grid in x-direction. Results imply that infinitely long and diffused shear layer results are in a good agreement in all regions other than high angles. Shear layer at the duct lip where sound radiation passes is thin. So, radiation directivity is not so much effected by shear layer.

This study applies Buffer zone of two types, explicit damping and a new damping type developed. Present Buffer zone are analyzed for different flow conditions. The results for farfield radiation are in agreement with direct method application, that is also in frequency domain. Also stretched grid technique used behaves like a damping factor if effectively used as grid density decreases resolution of the amplitude decreases. Graded stretching is supplied through calculations of both mean flow and acoustic field. Numerical results show that buffer zone farfield results are in a similar trade with direct method results. Buffer zone application has lower amplitude loss characteristic by absorbing spurious waves. Also, Results imply that characteristic based boundary conditions are not efficient for the modes that are nearly cut-off. So, one must be careful when using characteristic based boundary condition at fan exit for cut-off ratios near to 1, where reflections become stronger. Buffer zone is more effective for the modes that are nearly cut-off.

Farfield results of buffer zones in different length enforce that the efficiency of buffer zone increases with its length. The length of the buffer zone is chosen such that it captures enough length by looking at wave propagation pattern of the mode in the duct. So the mode resolution is captured and incidence field data is applied all over the buffer zone, minimizing reflection in the duct. From the results, it is showed that as the buffer zone length increases the amplitude loss decreases, showing the effect of reflection in the duct to radiation pattern of the mode outside the duct. Results of characteristic and buffer zone illustrate an agreement around maximum radiation peak but differ in amplitude.

Different Kirchhoff surfaces are placed around the duct to see the radiation pattern at different integration surfaces. Farfield characteristics of these surface shows similar pattern around maximum amplitude. Some differences in amplitude is seen around high angles. This is result of low grid density. In general, surface selection criteria applied for farfield predictions works with success. Amplitude and maximum radiation angle are nearly same for these compared cases. Results prove that farfield radiation of different Kirchhoff surface do not so much affected from mesh stretching for these cases.

Technological improvements in aerospace will enforce researchers to focus on radiation and propagation of acoustic sound and attenuate sound level. Because of their speed, Numerical approaches will be widely used for technical developments, enforcing researches to find faster 3-D solutions with nonuniform background flow. Improving computer technology and new acoustical approaches will ease these developments, such as direct methods, multigrid applications and etc. With the help of these contributions, limitations caused by the assumptions for specific sound propagation can be completely eliminated.

REFERENCES

[1] Brown, Alan S., *Aerospace America* , February 2000, pp.26

[2] Kerrebrock, Jack L., *Aircraft Engines and Gas Turbines*, The MIT Press, 6th press,1984

[3] Ffowcs Williams, J.E., *Aeroacoustic*, Journal Of Sound and Vibration, 1996,190 (3),pp. 387-398.

[4] Advanced Topics in Aerodynamics Web Page, *URL:http://aerodyn.org/aero.html*, Last access date: 03/09/2005

[5] Depitre, A., *Aircraft Noise Certification History/Development*, Noise Certification Workshop,

[6] Aerospace Industries Association Web Page, *URL:http://www.aia-aerospace.org*, Last access date : 10/11/2005

[7] Farassat F., Myers M.K., *Extension of Kirchhoff's formula for radiation for moving surfaces*, Journal of Sound and Vibration, Vol. 123, 1988, pp. 451-460.

[8] Taylor, R., Liu, F., Horowitz, S., Ngo K., Nishida, T., Cattafesta, L., Sheplak, M., *Technology Development for Electromechanical Acoustic Liners*, ACTIVE 04, Williamsburg, Virginia, 2004 September 20-22.

[9] Preisser J.S., Chestnutt D., *Flight Effects on Fan Noise with static and Wind Tunnel Comparisons*, NASA Langsley Research Center, AIAA 8th Aeroacoustic conference, AIAA-83-0678 (1983).

[10] Schoenster, J.A., *Fluctuating Pressure Measurements on the Fan Blades of a turbofan Engine During groung ang flight tests*, NASA Langsley Research Center, AIAA 8th Aeroacoustic Conference, AIAA-83-0679 (1983).

[11] Benzakein, M.J., *Research on Fan Noise Generation*, The Journal Of Acoustical Society of America Vol. 51,No. 5 (PT1),1972.

[12] Philbicrick D.A., Topol D.A., *Development of a Fan Noise Design System Part 1 : System Design and Source Modelling*, 15th AIAA Aeroacoustic Conference, AIAA-93-4415, 1993.

[13] Tyler,J.M. and Sofrin, T.G., *Axial Flow Compressor Studies*, SAE Transactions, Vol.70, 1962, pp. 309-332.

[14] Long, D.F., *A Nozzle Test Stand for Simultaneous Measurement of Thrust and Radiated Noise*, AIAA/ASME/SAE/ASEE Joint Propulsion Conference and Exhibit, 34th, Cleveland, OH, July 13-15, 1998 AIAA-1998-3108.

[15] Gloerfelty, X., Bogeyz, C., Baillyx, C., Juv, D., *Aerodynamic noise induced by laminar and turbulent boundary layers over rectangular cavities*, *8th* AIAA/CEAS AeroAcoustics Conference, Athens, Greece AIAA 2002-2476.

[16] Özyörük, Y. and Long, L.N., *Time-domain calculation of sound propagation in lined ducts with sheared flows*, 5*th* AIAA/CEAS Aeroacoustics Conference,Bellevue, Washington AIAA Paper 99-1817.

[17] Raman, G., *Highlights of Aeroacoustic Research in U.S. 1998*, Journal of Sound and Vibration, Vol. 228(3), 1999, pp.589-610.

[18] Lighthill, M.J., *Sound Generated Aerodynamically: 1.General theory*, 1952 Proceedings of the Royal Society, London A221(1107),564-587.

[19] Miller, C.J., Dittmar, James H., Jeracki, R., *Ultra high bypass research in Aeropropulsion*, NASA Resarch Center, (1991), NASA conference Publication 10063, N91-20117.

[20] Clark,L.R., Thomas,R.H., Dougherty,R.P., Farasat,F. and Gerhold,C.H., *Inlet Shape effects on the Far-field Sound of a model fan*, 3rd AIAA/CEAS Aeroacoustic Conference, AIAA Paper No. 97-1589.

[21] Weir, D., and Marsan, M., *Estimation of Full Scale Turbofan Engine Noise from Scale Model Fan Rig Measurements*, 15th Aeroacoustic Conference, AIAA Paper No.93-4419.

[22] Nallasamy, M., Sutliff, D.L., Heidelberg, L.J., *Propagation of Spinning Acoustic Modes in Turbofan Exhaust Ducts*, Journal of Propulsion and power, Vol. 16,No. 5, 2000.

[23] Eversman, W., Okunbur, D., *Aft fan duct acoustic radiation*, Journal of Sound and Vibration, 213(2), 1998, pp. 235-257.

[24] Bailly, C., Bchara, W., Lafon, P., *Jet Noise Predictions Using a K-epsilon Turbulence Model*, 15th AIAA Aeroacoustic Conference, AIAA Paper No. 93-4412.

[25] Roy, D., *Doppler Frequency Effects due to source, Medium and Receiver Motions of Constant Velocity*, AIAA 8th Aeroacoustic Conference, AIAA Paper No. 83-0702.

[26] Tam, C.K.W., Kurbatskii, K.A., *Microfluid Dynamics and Acoustics of Resonant Liners*, AIAA Journal, Vol.38 No.8, 2000, pp.1331-1339.

[27] Morin, B.L., *Broadband Fan Noise Prediction System for a gas turbine engines*, 5th AIAA/CEAS Aeroacoustic Conference, AIAA Paper No. 99-1889,

[28] Özyörük, Y., *AEE-548 Lecture Notes, Middle East Technical University*, , 2001.

[29] Powell, A., *Lord Rayleigh's foundations of aeroacoustics* , Acoustical Society of America, 98(4), October 1995, pp. 1839-1844.

[30] Tam, C.K.W., and Webb, *Dispersion-Relation-Preserving Difference Schemes for Computationla Acoustics*, Journal of Computational Physics, Vol.107, No.2, 1993, pp. 262-281.

[31] Hu, F.Q., Hussaini, M.Y., Manthey, J.L., *Low-Dissipation an Low-Dispersion Runge-Kutta Schemes for Computational Aeroacoustics*, Journal of Computational Physics, No. 124, pp. 177-191 (1996).

[32] Giles, M.B, *Nonreflecting boundary conditions for Euler Equation Calculation*, AIAA Journal, Vol.28, No.12, 1990, pp.2050-2058.

[33] Bayliss, A., *Far Field Boundary Conditions for Compressible Flows*, Journal of Computational Physics, Vol. 48 (1982), pp. 182-189.

[34] Zang, X., Chen, X.X., Morfey, C.L. and Tester, B.J., *Computation of Fan Noise Radiation through A Realistic Engine Exhaust Geometry with Flow*, 9th AIAA/CEAS Aeroacoustics Conference and Exhibit, Hilton Head, South Carolina, May $12-14$, 2003 AIAA-2003-3267.

[35] Thompson, K.W., *Time dependent boundary conditions for hyperbolic systems II*, Journal of Computational Physics, Vol.89, Issue 2, pp. 439-61.

[36] Myers, M.K., *On the acoustic boundary conditions in the presence of flow*, Journal of Sound and Vibration, 71(3), pp.429-434, 1980.

[37] Özyörük, Y., Long L.N., *Impedance Boundary Conditions for Time-Domain Computational Aeroacoustic Methods*, 35th Aerospace Sciences Meeting and Exhibit, 1997. AIAA Paper No. 97-0021.

[38] Özyörük, Y., Alpman, E., Ahuja, V., Long, L.N., *Frequency-Domain prediction of turbofan noise radiation*, Journal of Sound and Vibration, Volume 270, Issue 4-5, pp. 933-950.

[39] Özyörük Y., Ahuja V., *Numerical Simulation of Fore and Aft Sound Fields of a Turbofan*, AIAA Journal, Vol.42, No.9, 2004.

[40] Özyörük Y., Ahuja V., Long L.N., *Time Domain Simulations of Radiation from Ducted Fans with Liners*, 7th AIAA/CEAS Aeroacoustics Conference, 2001, AIAA 2001-2171.

[41] Özyörük Y., Long L.N., *Multigrid Acceleration of a High-Resolution Computational Aeroacoustic Scheme*, AIAA Journal, Vol.35,No.3,1997

[42] Long N.L., *A nonconservative nonlinear flowfield splitting method for 3-D Unsteady Fluid Dynamics*, 6th AIAA/CEAS Aeroacoustics Conference, AIAA Paper No. 2000-1998.

[43] Dougherty R.P., *Nacelle Acoustic Design by Ray Tracing in Three Dimensions*, 2nd AIAA/CEAS Aeroacoustics Conference, AIAA Paper No. 96-1773.

[44] Philbrick D.A., Topol D.A., *Development of Fan Noise Design System Part 1: Design System and Source Modelling*, 15th Aeracoustic Conference, AIAA Paper No. 93-4415.

[45] Glegg S.A.L, Jochault C., *Broadband Self Noise from a Ducted Fan*, 3rd AIAA/CEAS Aeroacoustic Conference, 1997, AIAA-1997-1612.

[46] Parrett, A.V., Eversman, W., *., Wave Envelope and Finite Element Approximations for Turbofan Noise Radiation in Flight*, AIAA Journal Vol. 24, pp. 753-760, (1986).

[47] Dunne,R.C., Howe, M.S., *Wall-bounded Blade Tip Vortex Interaction Noise*, Journal of Sound and Vibration, 202(5), pp. 605-618.

[48] Nallasamy, M., Envia, E., *Computation of Rotor Wake Turbulance*, Journal of Sound and Vibration 282 (2005), pp. 649-678.

[49] El-Fadel, M., Chahine, M., *Case History: An assessment of the economical impact of airport noise emissions near Beirut Airport*, Noise Control Engineering Journal, Vol.50(1), pp. 36, 2002 Jan-Feb.

[50] Zhang, X., Chen, X.X., Morfey, C.L., Nelson, P.A., *Computation of Spinning Modal Radiation from an Unflanged Duct*, AIAA Journal, Vol.42, No.9, September 2004.

[51] Brentner,K.S. , Farassat,F., *An Analytical Comparison of the Acoustic Analogy and Kirchhoff for Moving Surfaces*, American Helicopter Society 53rd Annual Forum, Virginia, April 29 - May 1, 1997, pp. 10.

[52] Geist, A., Beguelin, A., Dongarra, J., Manchek, R. and Sunderam, V., , Oak Ridge National Laboratory, Tennessee, 1994

[53] Fang, Q. Hu, *Absorbing Boundary Conditions*, International Journal of Computational Fluid Dynamics August 2004 Vol. 18 (6), pp. 513-522.

[54] Atlantic Flight Training, *Jeppesen JAR ATPL (A) 2005 Manuals Powerplant Book*, April 2005 press.

[55] Montgomery, S., *Engine Noise Reduction Programme; making aircraft engines better neighbours*, Airbus Technology Magazine - FAST 37 Flight Airworthiness Support Technology, December 2005.

[56] Engineering Sciences Data Unit Web Page, *URL:http://www.esdu.com*, Last access date: 02/08/2005

[57] Advanced Topics in Aerodynamics Web Page, *URL:http://www.aircraftenginedesign.com*, Last access date: 27/08/2005